PNAS
www.pnas.org

Supplementary Information for

Increasing and widespread vulnerability of intact tropical rainforests to repeated droughts

Shengli Tao*, Jérôme Chave*, Pierre-Louis Frison, Thuy Le Toan, Philippe Ciais, Jingyun Fang, Jean-Pierre Wigneron, Maurizio Santoro, Hui Yang, Xiaojun Li, Nicolas Labrière, Sassan Saatchi

*Correspondence to: sltao@pku.edu.cn; jerome.chave@univ-tlse3.fr

This PDF file includes:

SI Materials and Methods

SI Materials and Methods

1. Microwave signal in ecological monitoring

Microwaves are electromagnetic waves with wavelengths ranging from ~1 mm to ~1 m (*1*). There are generally two types of microwave sensors: passive (radiometer) and active (radar). Since objects much smaller than the wavelength are invisible to microwaves, the microwave signal can penetrate surfaces (such as the forest canopy) to some extent, with the penetration depth increasing with increasing wavelength. Microwaves are not affected by clouds and raindrops over tropical rainforests, given a wavelength much larger than the size of raindrops, such as ~6 cm (or, C-band radio frequency; *1*). Microwave data, especially those with a relatively long wavelength, are therefore suitable for monitoring changes in tropical forests. The spaceborne radar sensors used in this study are Earth-pointing active microwave instruments that transmit pulses of microwave radiation and record the signal backscattered from the Earth's surface along the line of sight of the instrument (*1, 2*). The signal intensity measured by active sensors is higher than that of passive sensors, the latter measuring the microwave signal naturally emitted by the Earth's surface.

When microwave signals interact with canopies, the amount of water molecules contained in the leaves and branches, i.e., their dielectric properties, affects the backscattered signals. This amount of water is the total mass of water in the leaves and branches, which depends on the density of leaves and branches (i.e., dry biomass) and their water content (mass of water per unit mass of dry biomass) (*1, 3*). Thus, whether the temporal changes in microwave signals reflect dynamics of canopy structure or tissue moisture dynamics requires careful interpretation. On diurnal and seasonal time scales, it can be assumed that the change in canopy structure is small, and the dynamics of microwave signal represents the change in forest moisture (*3*). Over many years, in addition to moisture, changes in canopy structure could explain long-term trends in the microwave signal (*3*) caused by the mixed effects of forest growth, mortality, and possibly also long-term changes in forest species composition. Sections 12-17 below further explore the influence of various factors on the radar signal.

2. Satellite radar data and pre-processing

The backscatter of the radar signal, usually expressed in decibels (dB), is a function of the sensor parameters (frequency, polarization, look angle and spatial resolution), and the dielectric (as detailed above) and geometric properties of the scattering objects. Spaceborne

radars used for Earth observation currently operate in a wavelength (λ) range between ~1 cm and 23 cm. Future radar sensors will operate with a wavelength of ~70 cm (*4*). For a forest, radar waves at $\lambda \approx 6$ cm (C-band) interact with leaves, twigs, and small branches thereby penetrating the top few meters of the canopy (*5*), whereas at $\lambda \approx 70$ cm the waves interact with larger branches and trunks and can reach the forest floor (*1*).

Satellite-based active microwave sensors include Synthetic Aperture Radar (SAR) which maps the backscattered signal into high spatial resolution images, and scatterometers which provide data at footprints with a coarser spatial resolution (> 1 km), but with a much higher revisit rate. This last property makes scatterometers interesting for the study of large-scale land surface dynamics. Spaceborne radar sensors have been deployed since 1978 (NASA's Seasat), but global radar coverage dates back to the European Remote Sensing satellite (ERS) in the 1990s (*5-8*). Over the last three decades, multiple missions have been launched with the aim of obtaining full and repeated global coverage (*9, 10*).

For this study, we considered the contribution of all data sets acquired by satellites flying a radar instrument, with repeated observations over at least one decade and with a wavelength longer than 1 cm to avoid issues related to cloud cover and rainfall. Scatterometer data from the European Remote sensing Satellite (ERS) -1/-2 operating at $\lambda \approx 6$ cm wavelength (C-band, from 1992 to 2001), the Advanced Scatterometer (ASCAT, C-band, from 2007 to 2018), and the Quik Scatterometer (QSCAT, operating at Ku-band, i.e., $\lambda \approx 2$ cm, from 1999 to 2009) were our primary candidates. In addition, we considered the use of data acquired by the ERS Synthetic Aperture Radar (SAR) (C-band, 1992 to 2011), the Advanced Synthetic Aperture Radar (ASAR, C-band, 2002 to 2012), Oceansat-2 Scatterometer (OSCAT, Ku-band, since 2009), the Radarsat-1 and -2 SAR (C-band, 1995–now), and the Sentinel-1A and -1B SAR (C-band, since 2014).

We found that data from the following four scatterometers together provided the longest time series of 27 years, namely ERS-1/-2 scatterometers (1992–2001, C-band), QSCAT (1999–2009, Ku-band), and ASCAT (2007–2018, C-band). A single time series at C-band would have been ideal, but reduced operations of the ERS-2 scatterometers began in 2001 (*11*). We therefore sought to fill the gap in the C-band data with Ku-band QSCAT data. In theory, the Ku-band signal interacts more with the smaller vegetation elements in the upper canopy layer (e.g., leaves) than the C-band signal, as the latter penetrates deeper into the canopy (*1*). However, we found that the Ku-band QSCAT signal can be adjusted to the ERS

observations during 1999–2001 and to the ASCAT observations during 2007–2009 to obtain a simulated C-band signal (see sections 5 & 6 for more details). We didn't use the Ku-band OSCAT as it operates in an overlapping period with ASCAT but has a shorter wavelength.

ERS-1/-2 scatterometer data were downloaded from the European Organisation for the Exploitation of Meteorological Satellites (EUMETSAT) while QSCAT (H-Polarization) and ASCAT (V-Polarization) data were available from the Center for Remote sensing at Brigham Young University (BYU). The latter provides images synthesised from acquisitions made over periods of five consecutive days. Ascending path images were used for QSCAT and ASCAT, and all path images for ERS-1/-2, thus guaranteeing the highest possible spatial and temporal coverages. Descending path ASCAT images and V-Polarization QSCAT images gave similar decreasing trends in radar signal. Since the radar backscattered signal was acquired under different look geometries, we normalized the observations to a common 40-degree incidence angle to be free of angle influence on the observations (*5*). The radar observations were averaged into monthly layers with a global coverage at a spatial resolution of 25 × 25 km. Some ASCAT images were characterized by regions with a low number of radar observations (Fig. S31a). These locations were set to "not-a-number" after thresholding for a minimum number of observations, which was set to 20. A few ERS images had large areas of data gaps and were removed from our data set (Fig. S31b). The ERS-2 sensor experienced a sensor drift of 0.2 dB from July 1996 to June 1997 in our study region (*12*), which was corrected during our processing.

3. Exploring alternative microwave data sets

To complement the scatterometer data sets and, possibly, fill gaps in space and in time, we also explored archives of other satellite observations at C-band. However, the ERS-1/-2 SAR and the Radarsat-1/2 SAR did not achieve complete and repeated coverage throughout their missions (*11*). The ASAR data sets were more homogeneous in space and time but lacked observations for tropical Asia between 2002 and 2010, and were in general poorly calibrated. Because of the temporally dense set of observations by ASCAT, the contribution of Sentinel-1 SAR data was not considered. The deficiencies of the SAR data sets here explored forced us to conclude that these could not act as an effective complement to the scatterometer data sets.

A further investigation was undertaken to see if passive microwave data could fill the data gap. C-band passive microwave data from the AMSR-E sensor operated between 2002 and 2011 (*13*), thus not overlapping with ERS. Data from another C-band passive microwave sensor, AMSR2, are available since 2012 and do not overlap with AMSR-E (*13*). AMSR-E and AMSR2 also provide passive microwave data at X-band (10.6 GHz) but merging them has been proven as difficult (*14*) because of the disconnection between the two sensors. Passive microwave data at even higher frequencies (such as Ku-band, 12.5 GHz) covered a relatively long timespan (*13, 15, 16*) but can be sensitive to atmospheric corrections. We therefore decided not to use passive microwave data in our analysis.

4. Definition of intact tropical rainforest

We restricted our analyses to the intact evergreen tropical rainforests. First, we defined evergreen tropical rainforests using the 2015 Climate Change Initiative (CCI) land-cover map, with a spatial resolution of 300 metres. A 25 km radar pixel was labelled as evergreen if more than 50% of the CCI land-cover pixels were evergreen forest (classes labeled as: 50, 160, 170 in the data set). To avoid confounding effects of land-use changes, we then defined intact tropical rainforests using the recently published 2020 baseline map of undisturbed tropical forests by Vancutsem et al. (*17*, 30 m resolution). Vancutsem et al. mapped deforestation and degradation events between 1990 and 2019 through combining big data information extraction and visual analytics aided by expert knowledge. The 2020 baseline map of undisturbed tropical forest contains the pixels fully covered with forests and have never been deforested or degraded during 1990-2019. A 25 km radar pixel was classified as intact tropical rainforest if the proportion of the 30 m undisturbed rainforest pixels within it was at least 95%. This filtering resulted in approximately 3800 pixels (about 2.4 million km^2) in the American tropics, 1100 (about 0.7 million km^2) in Africa and 430 (about 0.3 million km^2) in Asia.

5. Scaling radar time series

We developed a two-step approach to harmonise C-band (ERS-1/-2 and ASCAT) and Ku-band (QSCAT) data into a continuous long-term radar data set. The first step was to produce uniform ranges of backscatter values from different sensors (i.e., data scaling). The second

step was to harmonise the scaled data into a smooth time series by processing their monthly differences, as follows.

We used the linear scaling method for rescaling time series. The linear scaling method involves first scaling a time series within the range of the reference time series, and then applying a linear regression equation between the two to minimise errors. We chose ASCAT as the baseline for the scaling because it has the best radiometric quality (lower sensitivity, higher radiometric resolution), and because it is still operational. The scaling procedure was performed pixel by pixel at a monthly time step. Specifically, a linear regression was established for each pixel using QSCAT and ASCAT data in the overlapping periods in 2007–2009, which we then applied to the entire time series of QSCAT data. Thereafter, the ERS data were mean-shifted to match the QSCAT-ASCAT time series (*18*). The ERS-1 and ERS-2 data sets were already calibrated, so there was no need to rescale them separately. Figure S27 shows an example of data scaling, where radar data from different sensors have been successfully unified into one scale.

6. Harmonising radar data

The scaled radar data were then harmonised into a smooth time series. Differences were found between C-band and scaled Ku-band signals, despite similar interannual variations (Fig. S28). It is important to note that the differences showed a seasonal pattern. During dry periods, Ku-band radar signals were higher than C-band, but in the wet periods they were lower (*19, 20*). The differences were most evident in regions with higher annual precipitation (Fig. S28). To account for the seasonality of the signal, we investigated the role of rainfall amount as a predictor. We calculated the monthly differences of C-band minus Ku-band signals during the overlapping periods (Fig. S29a). We then regressed the signal differences against monthly precipitation measured by the TRMM (Tropical Rainfall Measurement Mission) 3B43 V7 data (Fig. S29b; *21*) and predicted the signal differences. CHIRPS rainfall data was also tested, and highly similar results were obtained (Fig. S29d-f). Finally, we added the predicted differences to the original Ku-band signals (Fig. S29c). This procedure resulted in a much-improved match between C-band and Ku-band signals. Some poor-quality pixels (less than 10%) were concentrated in northwest Amazonia and the Asian tropics, where precipitation has no clear seasonality and signal differences consequently showed no clear temporal pattern (Fig. S30a). We therefore used the Decision Tree regression to capture the

non-linear relationship between signal differences and precipitation (*22*), and this improved the goodness of match in these pixels (Fig. S30, d & e). Quality assessment indicates a global median r value of 0.62 between C-band and corrected Ku-band signals in the overlapping years (1999-2001 and 2007-2009). For the pixels where Decision Tree regression was used to model the signal differences, their final median r value is 0.61.

Lastly, the regression (linear or decision tree) between the signal differences and precipitation, established with data from the overlapping periods, was applied on TRMM precipitation data from 1999 to 2009, and the predicted signal differences were added to the full QSCAT time series. The data merging procedure was applied pixel by pixel. After transforming the QSCAT data, we built a time series for each pixel for the 1992–2018 period, averaging data from the overlapping periods (1999–2001 and 2007–2009).

7. Validation of the time series construction method

From January 2001 to 2011, the ERS-2 satellite experienced a series of failures that affected data continuity and global coverage. However, observations were occasionally available over some tropical regions (*11*), which allowed us to test whether the scaled Ku-band (QSCAT) signal is consistent with the C-band signal. We used the European Space Agency (ESA) reprocessed ERS-2 data set covering the period of 1996–2011 (https://earth.esa.int/web/guest/missions/esa-operational-eo-missions/ers/news/-/article/ers-2-scatterometer-l2-dataset-processing-with-asps-v-10-04-completed). Part of the American and Asian tropics were covered by this ERS-2-ESA data set, and we compared it to our merged radar data set in these two regions. Monthly radar backscatter coefficients at 40-degree incidence angle were calculated from the ERS-2-ESA data set, and compared with our merged radar data set. Both in tropical Americas and Asia, we found similar backscatter dynamics between ERS-2-ESA and our merged data (Pearson $r \geqslant 0.88$, Fig. S3), validating our data merging approach.

We also compared the radar signal over different land-cover types where its seasonal amplitude is expected to be very different. We confirmed that the backscatter signal was lower in shrubland, savanna and deciduous forest than in evergreen rainforest, and that, as expected, the drier biome types displayed a higher seasonality than the evergreen forests (Fig. S2).

8. Influence of spatial autocorrelation on the significance of signal trends

The decreasing trends in radar signal shown in Fig. 1 were averaged across pixels per continent. However, we expect radar signals to be correlated from pixel to pixel. This could imply a spatial pseudo-replication in some of the trend analyses: trend results may appear falsely significant because of an over-inflated sample size. We thus tested whether the decreasing radar trends are robust to spatial autocorrelation.

We used the following approach:

1. randomly select N pixel pairs in each continent, each pair containing two pixels with a distance D of 0.25 (in degree unit, the size of radar pixel). N was set at 1/10 of the total number of pixel pairs with a distance D.
2. calculate the Pearson r between pairs of radar time series, and then average r across all pairs. Repeat these two steps 500 times, and take the mean values.
3. vary D by increments of 0.25 degrees, and record the D values and mean r values.
4. plot the mean r values against D values, to identify the geographical distance (D2) corresponding to a mean Pearson r of 0.5.

Once the spatial autocorrelation D2 was known, we selected a subset of pixels at least D2 apart (15, 24, and 52 pixels in tropical Americas, Africa, and Asia, respectively), and recalculated the average radar signal trend over this reduced sample. This reanalysis resulted in very similar results for the signal trends calculated as average across all pixels and those averaged across the reduced sample of pixels (Pearson $r \geq 0.92$, Fig. S6). This result confirms that the significant decreasing trend in radar signal found in this study is not caused by autocorrelation.

9. Definition of past droughts

Quantifying drought events across regions is difficult (*23*), especially in tropical rainforests where climate stations are scarce. The cumulative water deficit (CWD) is a useful metric for defining droughts in the tropics (*23, 24*). CWD was calculated at a monthly time-step as the cumulative difference between precipitation (*P*) and evapotranspiration (*E*). The cumulative water deficit (CWD) is always negative or equal to zero, and is defined as:

220 $if \quad CWD_{n-1}\text{-}E+P<0$

221 $then \quad CWD_n = CWD_{n-1}\text{-}E+P$

222 $else \quad CWD_n=0$

223 Precipitation *P* was taken from the CHIRPS data (*25*) because TRMM was unavailable
224 between 1992 and 1998. The CHIRPS data set was created by integrating satellite
225 observation with *in situ* rain gauge data (*25*). During the period 1998–2018, the CHIRPS
226 precipitation product was similar to the TRMM product, but the former was extended through
227 the period 1992–2018 in our analysis. Previous research has assumed a monthly value of 100
228 mm for tropical rainforest evapotranspiration, *E* (*24*). Here, to better accounts for soil and
229 atmosphere water stresses across regions, we used an improved version of CWD, with *E*
230 taken from the long-term Global Land Evaporation Amsterdam Model (GLEAM) product,
231 version 3.3a (https://www.gleam.eu/) (*26*; Fig. S4).

232 To identify past drought events, we then computed the standardized anomaly (or Z-score)
233 of the maximum *CWD* in a year ($Z_{MCWD,y}$):

234 $$Z_{MCWD,y} = \frac{\max_y(CWD) - \overline{\max_{refer}(CWD)}}{\sigma_{\max_{refer}(CWD)}}$$

235 where $\max_y(CWD)$ is the maximum of the cumulative water deficit in year *y*,
236 $\overline{\max_{refer}(CWD)}$ is the average of $\max(CWD)$ during a reference period, and $\sigma_{\max_{refer}(CWD)}$
237 is the standard deviation of $\max(CWD)$ during the same reference period. The reference
238 period covers all the years excepted the year under study (*27*). The calculation was performed
239 at pixel level and for each year of the period 1992-2018. A threshold of -1 on $Z_{MCWD,y}$ was
240 then used to decide whether a pixel was exposed to an anomalous drought in year *y*. The
241 drought severity was finally calculated as the absolute value of $Z_{MCWD,y}$.

242

243 10. Trend analysis of forest response

244 The temporal radar signals were averaged over continental pixels (Fig. 1). To clearly show
245 the long-term changes in radar signal, a 12-month moving average was calculated (thick lines
246 in Fig. 1). Annual rates of radar signal change were then calculated as the slopes of the linear
247 fits to monthly radar signals (equations labelled in Fig. 1). The linear fit was also applied at
248 the pixel level to obtain the annual rate of radar signal change of each pixel (Fig. 2).

The BFAST (Breaks For Additive Season and Trend) algorithm was then used to check whether drought events had caused "breaks" in radar time series (Fig. S5). BFAST detects "breaks" in a time series by fitting piecewise linear models iteratively to different sections of the time series (*28*). Correlations between radar time series and water deficit were then calculated at pixel level (Fig. S8). We also explored the dependence on land surface temperature (T_s) as both water deficit and (T_s) could force vegetation stress (*29*). Diurnal (T_s) data were extracted from the MODIS database from 2002 to 2018. We also correlated the radar signal with air temperature (ERA5-Land; DOI: 10.24381/cds.68d2bb30; *30*).

11. Drought resistance and resilience of intact tropical rainforests

Previous research has attempted to detect early-warning signals in non-linear systems, including with remotely sensed data (*31, 32*). Considering that meteorological conditions changes from year to year, here we used short-term forest resilience and resistance to clearly see the response of forests to each drought event. Drought resistance and resilience were defined, respectively, as:

$$resistance = \frac{Y_e - Y_{pre}}{Y_{pre}}$$

$$resilience = \frac{Y_{post} - Y_{pre}}{Y_{pre}}$$

Where Y_e is the minimum radar data during a drought event, i.e., the extent of radar signal reduction during a drought, and Y_{pre} and Y_{post} are the maximum radar values before and after a drought event, respectively. These definitions are directly inspired by Lloret et al (*33*).

For each forest pixel, we detected drought events in that pixel based on the basis of the standardized anomaly (Z-score) of MCWD. As described above, a pixel was considered to have experienced a drought in a year if the Z-score of MCWD reached a value lower than -1, and drought severity was calculated as the absolute value of the Z-score of MCWD. For the year in which a drought occurred, we then identified the month when drought intensity reached its maximum. Y_e was then calculated by looking for the minimum radar value within a three-month range centred on the month when drought intensity reached its maximum, considering that there might be a time-lag between a drought and forest response. Y_{pre} was calculated as the maximum radar value within the two years prior to the drought, and Y_{post} was calculated as the maximum radar values in the two years after the event, because

previous research has reported a drought legacy effect of two years in rainforests (*34*). This also avoids the situation where the year prior to the drought was also droughted, thus leading to an overestimation of drought resilience. We used radar signal maxima before and after the drought because they correspond to wet-season conditions, and thus have comparable moisture levels, their difference (namely, resilience) thus measures forest structure changes from canopy disturbance, rather than moisture changes.

The amplitudes of the radar signal vary across regions, and we therefore also rescaled the radar time series to fall into the range 1-100 for each pixel before calculating the resistance and resilience indices. By definition, resistance and resilience could not be calculated for the droughts occurring in the first (1992) and the last year (2018) of the study period. In the tropical Americas, only six months in the year of 1998 had qualifying radar observations, hence we did not calculate drought resistance and resilience in 1998 for the tropical Americas. Resistance and resilience associated with all other drought events were calculated at the pixel scale, and were further summarized in continents (Figs. 3 & 4).

The Mann-Kendall trend test, a classical nonparametric test for identifying trends in time series data, was used to check whether there are significant trends in the drought resistance/resilience time series (Figs. 3 & 4; *35*). Kendall's tau, or τ, indicates whether a trend exists. The value of τ ranges from -1 (negative trend) to 1 (positive trend). A trend is considered strong if the absolute value of τ is close to 1. The significance of the trend was judged by a two-sided P value. We used the R package 'Kendall 'for Mann-Kendall test (https://cran.r-project.org/web/packages/Kendall/index.html). As the Mann-Kendall test has a requirement on the length of the input time series that cannot be satisfied at the pixel level, we used Spearman's rho (SR) test (*36*) to check the temporal changes in resistance/resilience in pixels where more than two droughts occurred during the study period (Fig. S16). Spearman's rho test is a rank-based method widely used for trend analysis, and its value also ranges from -1 (strong negative trend) to 1 (strong positive trend). We used Matlab R2018 to evaluate Spearman's rho test.

We checked that our conclusion was not altered by the use of a longer drought legacy window, a lower threshold for Z-score of MCWD, a constant evapotranspiration of 100 mm per month (*24*), and detrended radar signals (Figs. S10-S13). The results of these sensitivity tests consistently indicated an increasing vulnerability of intact rainforests to drought, especially in the tropical Americas. The conclusion was also verified when the monthly CRU Self-calibrating Palmer Drought Severity Index (scPDSI) was used instead of the Z-score of

MCWD to identify past drought events (Fig. S14; *37*). A threshold of -1 was applied on scPDSI to define droughts, and the absolute value of the minimum scPDSI value during droughted months was used as a quantification of drought severity.

12. Interpreting the long-term radar signal declines: Sensitivity of C-band radar data to forest degradation/deforestation

We found sustained declining trends in radar signal over the past decades in all three continents. To interpret the sustained declines in radar signal, we analysed possible drivers of radar signal change. We first assessed the sensitivity of C-band radar data to forest degradation/deforestation, using three approaches.

In the first approach, we grouped the intact tropical rainforest radar pixels into different categories of forest degradation or deforestation intensities, namely less than 1%, 1-2%, 2-3% and 3-5% (cumulative degradation/deforestation ratio between 1992 and 2018). The degradation/deforestation information were derived from the Vancutsem et al. maps (*17*). If degradation or deforestation had contributed to the radar signal trend, we would expect a steeper slope in the 3-5% class than in the <1% class. However, we found that the radar anomaly showed a similar decline in all four classes of degradation/deforestation in tropical Americas. In tropical Africa and Asia, pixels with a 3-5% degradation/deforestation ratio even showed less severe declines in radar anomaly than in the <1% class (Fig. S19). This shows that the long-term decline in radar signal was not driven by the small fraction (<5%) of degradation/deforestation within the intact rainforest radar pixels.

Secondly, we used pixels with an increasing trend in radar signal as a test set, in tropical Americas and Africa. Too few pixels showed an increasing trend in radar signal in tropical Asia, so this continent was not included in the analysis. One possible hypothesis is that the pixels with an increasing trend in radar signal cover the true intact tropical forests, and that all other forests are exposed to some form of deforestation or degradation explaining the decline in radar signal. Using Vancutsem et al.'s maps (*17*), we explored the temporal dynamics of degradation/deforestation intensity for pixels with decreasing radar trends, and we compared these with the degradation/deforestation intensity in pixels with increasing radar trends. We found no difference in the pattern of degradation/deforestation intensity in the two groups of pixels (Fig. S7). In contrast, water stress explained the differences: the pixels with an increasing radar signal trend experienced much less severe water deficit during

2005-2014, which corresponds to the period when one time series declined while the other remained relatively stable (Fig. S7). This phenomenon was observed in both tropical Americas and Africa. The results are therefore consistent with the hypothesis that droughts rather than degradation/deforestation dominate changes in the radar signal.

Lastly, we verified that other masks of intact tropical rainforest did not alter the findings. We used Hansen et al's (*38*) forest change maps between 2000 and 2018 and the Forest Integrity Index (FII) map which reflects the state of global forests for the year of 2019 (*39*). Using the forest-cover and annual degradation/deforestation maps from Hansen et al. (*38*, 30 m resolution), we created an intact rainforest mask at 25 km resolution as follows: all 30 m pixels were classified as intact tropical rainforest if they had >90% forest cover in 2000 and did not show any sign of deforestation from 2000 to 2018; a 25 km radar pixel was then classified as intact rainforest if the proportion of 30 m intact rainforest pixels within it was at least 90%. Using the Forest Integrity Index (FII, ~300 m resolution; *39*), we created a mask at 25 km resolution by selecting the radar pixels in which at least 90% of the FII pixels have a high integrity index (>9.6 as defined in ref *39*). We reached the same conclusion of a decline in radar signal irrespective of the selected mask (Fig. S20), confirming that the result is neither sensitive to the mask used to define intact tropical rainforests nor to the extent of residual degradation/deforestation found in radar pixels defined as "intact".

13. Interpreting the long-term radar signal declines: Sensitivity of C-band radar data to soil moisture

We tested whether the radar signal contained mainly canopy backscatter information, and that contributions from the ground through canopy gaps represented a minor fraction. To this end, we compared our radar data with the L-band time series ($\lambda \approx 20$ cm) of brightness temperatures from the Soil Moisture and Ocean Salinity (SMOS) radiometer. SMOS brightness temperature is more sensitive to soil moisture than C-band scatterometer signals (*40*). We used a "worst-case" scenario in which a severe flood occurred under a forest in southwestern Amazonia near the Beni savannas in Bolivia. As expected, the SMOS brightness temperature dropped suddenly during the flood, but C-band signal showed no abrupt change (Fig. S22), suggesting that the contribution of soil moisture to the C-band radar backscatter is negligible over dense tropical forests.

14. Interpreting the long-term radar signal declines: Influence of heavy rain events

Heavy rain (e.g., due to local thunderstorm) could reduce the backscatter by a few dB at C-band. However, heavy rain is often localized, thus its impact should become less severe at the scale of 25 km. Besides, the impact of heavy rain on radar signal is usually short, causing drops in radar backscatter that last less than a few days. Since we averaged the radar data into monthly composites, the effect of heavy rain on the radar signal used in our study is negligible.

To quantitatively assess the influence of heavy rain on radar signal, we calculated the temporal trends in rain rate (>5 mm/hour) observed at the time of the QSCAT acquisition (6:00 am of each day in 1999-2009) and ASCAT acquisition (21:30 pm of each day in 2007-2018), using TRMM 3B42 3-Hourly rainfall data (*41*). We found that globally 56% and 62% of intact rainforests showed decreasing trends in rain rate (>5 mm/hour) when QSCAT and ASCAT observations were acquired, respectively (Fig. S18). The spatial pattern contrasts with the observed widespread decline in radar signals. Thus, we concluded that the heavy rain events should not be responsible for the long-term radar signal decreases.

15. Interpreting the long-term radar signal declines: Shifts in dry season length

Previous research has detected a significant increase in dry season length in the rainforests of southern Amazonia (*42*) and Central Africa (*43*), and this could be a potential driver of the long-term radar signal change. We calculated the duration of the dry season using precipitation data from the GPCC (*44*; available until 2016), to be consistent with Jiang et al. (*43*). Mean yearly radar signal was correlated with dry season length between 1992 and 2016 in southern Amazonia but the relationships were mainly caused by extreme drought events (Fig. S21c). Thus, the effect of increase in dry season length on radar signal changes is insignificant.

16. Interpreting the long-term radar signal declines: Influences of leaf surface water

Leaf water is a key component of the canopy water content and has been reported to influence microwave signal. The influence was found to be most pronounced at the diurnal time scale (*45*). To clarify the role of leaf water changes on radar signal trends, we explored the long-term dynamics in leaf surface water (LWs, including dew and intercepted rainfall) and leaf internal water (LWi) —two components of leaf water content.

First, we tested whether the radar signal decreases reflect reduction in LWs. Both dynamics in dew duration and intercepted rainfall were explored. Intercepted rainfall correlates with monthly rainfall amount. Monthly dew duration was calculated as the percentage of hours within a month when air temperature is lower than dew-point temperature, with dew point temperature and air temperature provided by the ERA5 hourly climate data set. We found no evidence for a significant decrease in rainfall amount or dew duration except in Africa (Fig. S23). We noted that the temporal dynamics in dew duration in African rainforests did not coincide with the radar signal trend: the latter showed a sustained decline after 2004/2005 while dew duration increased during this period.

Second, we explored whether the decline in radar signal is driven by a decline in leaf internal water (LWi). Plant physiology constrains the moisture of a leaf: even small moisture loss within the leaf creates a loss of turgor and eventually leaf abscission (*45, 46*). Thus, LWi should not vary with time except for through changes in leaf amount (loss or gains of leaves). As a result, LWi changes can be indicated by changes in forest leaf amount. We used Normalized Difference Vegetation Index (NDVI) and Leaf Area Index (LAI) to explore the long-term changes in leaf amount in our study area. Since it is challenging to draw inferences from optical remote sensing images over tropical rainforests, we used four sets of NDVI/LAI products, including the Global Inventory Monitoring and Modeling System (GIMMS) third generation NDVI (available between 1981 and 2015; *47, 48*), GIMMS LAI3g (available between 1981 and 2016; *49*), GLOBMAP LAI (available between 1981 and 2020; *50*) and Moderate Resolution Imaging Spectroradiometer (MODIS) LAI (available since 2000). For GIMMS LAI and NDVI, we used the quality flag embedded in the data to include only the high-quality observations in the data analyses. MODIS LAI was also quality-controlled as in ref (*51*). We failed to detect trends in NDVI in all three continents. Regarding LAI, the three sets of LAI products differed in temporal dynamics, but they showed no sign of significantly sustained decrease since 1992 (Fig. S24). In Africa and Asia, GIMMS LAI decreased after 2010, but this temporal trajectory did not match with radar signal changes in Africa and Asia. More specifically, GIMMS LAI increased around 2004/2005 in Africa when radar signal started to decrease continuously (Fig. S24). GIMMS LAI was stable between 2000 and 2010 in Asia but radar signal decreased continuously during the same period.

Based on the above analyses, we concluded that neither leaf surface water nor leaf internal water are the drivers of the long-term declining radar signal trends.

17. Interpreting the long-term radar signal declines: Forest biomass changes

In addition to forest water stress, drought can also cause forest structure and biomass changes through, for example, drought-induced defoliation, branch fall, or tree mortality (*34, 52, 53*), thus influencing forest radar signals at the inter-annual or even longer time scales. We therefore also explored whether the long-term radar signal declines could correspond to drought-induced forest biomass changes. We first compared the radar signal trends with two long time series of forest aboveground biomass carbon data sets from Liu et al. (*54*) and Xu et al. (*55*), for the American tropics. The time series of forest carbon of Liu et al. was created mainly using Ku-band (19.3 GHz) and X-band (10.7 GHz) Vegetation Optical Depth (VOD) data. The Xu product was created using extensive forest inventory and multiply remote sensing data such as airborne laser scanning, satellite lidar measurements of vegetation height, and time series of microwave images. Our radar signal showed similar temporal trends with the two forest carbon time series (Fig. S25). The Pearson r value between the yearly radar signal and Xu carbon density is 0.86. The Pearson r value between the yearly radar signal and Liu carbon density is 0.84 (Fig. S25).

We then conducted a stricter comparison. We compared changes in the radar signal with plot biomass changes caused by the Amazon droughts of 2005 and 2010. For the 2005 drought, 55 RAINFOR plots with a median size of ca. 1 ha were censused before and after the drought (*23*), some in the same radar pixel. During the censuses, all trees $\geqslant$ 10 cm trunk diameter were measured, and new individuals were tagged and identified taxonomically. The census periods of plots varied: the median start date of the 2005 census periods of all plots was June 2004, and median end date was April 2006, with a variation of ~5 months in both cases. Therefore, to match these census periods, we used the maximum monthly radar value within a 5-month window centered at June 2004 (i.e., from April to August 2004) as the starting radar value, and the maximum value during February–June 2006 as the ending value. As with the calculation of the resistance/resilience index, the aim of using the maxima of the radar signal is to minimize the influence of moisture level variations on the trends in radar signal.

For the 2010 event, a total of 97 plots across Amazonia were available (*56*), also with a median size of ca. 1 ha. Changes in plot biomass caused by the 2010 drought were calculated as the anomalies with respect to a baseline average for 1998–2010 (*56*). This calculation can be readily applied to radar signals without the necessity of controlling for inter-census duration as for the 2005 plot data. Thus, we expect the comparison with the 2010 drought

474 ground data to be more reliable. We calculated the radar anomalies for the 2010 event the
475 same way as Feldpausch et al. (*56*) calculated the biomass anomalies. For both drought
476 events, plot data within the same radar pixel were averaged, and radar signals were smoothed
477 using a moving window of 3 months to improve robustness. Regression analyses were then
478 conducted using the standard major axis (SMA) regression implemented in the R package
479 "smatr" (*57*).

480 Significantly positive relationships between radar signal and plot biomass changes were
481 observed (Fig. S26a & b), although the R-squared values were low. As an attempt to address
482 the mismatch of scales between radar data (25 x 25 km) and plot data (1 ha), we included
483 only radar pixels with at least two ground plots, with inter-plot distance at least 5 km or 10
484 km (Fig. S26c & d). From this analysis, we concluded that although the radar signal measures
485 changes in the upper canopy, it not only captures drought-induced water stress but also
486 rainforest biomass dynamics at the inter-annual time scale.

References

1. Ulaby, F. T., Moore, R. K., Fung, A. K. Microwave Remote Sensing: Active and Passive. Addison Wesley, Advanced Book Program: Reading, Massachusetts (1982).
2. Steele-Dunne, S. C. *et al.,* Radar remote sensing of agricultural canopies: A review. *IEEE J-STARS* **10**, 2249–2273 (2017).
3. Konings, A. G., Rao, K., Steele-Dunne, S. C. Macro to micro: microwave remote sensing of plant water content for physiology and ecology. *New Phytol*. **223**, 1166–1172 (2019).
4. Le Toan, T. *et al.,* The BIOMASS mission: Mapping global forest biomass to better understand the terrestrial carbon cycle. *Remote Sens. Environ.* **115**, 2850–2860 (2011).
5. Frison, P. L., Mougin, E. Use of ERS-1 wind scatterometer data over land surfaces *IEEE Trans. Geosci. Remote Sens.* **34**, 550–560 (1996).
6. Wagner, W., Lemoine, G., Borgeaud, M., Rott, H. A Study of Vegetation Cover Effects on ERS Scatterometer Data. *IEEE Trans. Geosci. Remote Sens.* **37**, 938–948 (1999a).
7. Wagner, W., Noll, J., Borgeaud, M., Rott, H. Monitoring soil moisture over the Canadian Prairies with the ERS scatterometer. *IEEE Trans. Geosci. Remote Sens.* **37**, 206–216 (1999b).
8. Prigent, C., Matthews, E., Aires, F., Rossow, W. B. Remote sensing of global wetland dynamics with multiple satellite data sets. *Geophys. Res. Lett.* **28**, 4631–4634 (2001).
9. Wagner, W. *et al.,* Temporal stability of soil moisture and radar backscatter observed by the Advanced Synthetic Aperture Radar (ASAR). *Sensors* **8**, 1174–1197 (2008).
10. Malenovský, Z. *et al.,* Sentinels for science: Potential of Sentinel-1, -2, and-3 missions for scientific observations of ocean, cryosphere, and land. *Remote Sens. Environ.* **120**, 91–101 (2012).
11. Crapolicchio, R. *et al.,* ERS-2 scatterometer: Mission performances and current reprocessing achievements. *IEEE Trans. Geosci. Remote Sens.* **50**, 2427–2448 (2012).
12. Lecomte, P., Wagner, W. ERS wind scatterometer commissioning & in-flight calibration. European Space Agency-Publications-ESA SP **424**, 261–270 (1998).
13. Moesinger, L. *et al.,* The global long-term microwave Vegetation Optical Depth Climate Archive (VODCA). *Earth Syst. Sci. Data* **12**, 177–177 (2020).
14. Du, J. *et al.,* A global satellite environmental data record derived from AMSR-E and AMSR2 microwave earth observations. *Earth Syst. Sci. Data Discuss.* **9**, 791–808 (2017).

15. Liu, Y. Y. *et al.,* An analysis of spatiotemporal variations of soil and vegetation moisture from a 29-year satellite-derived data set over mainland Australia. *Water Resour. Res.* **45**, w07405 (2009).
16. Liu, Y. Y. *et al.,* Enhanced canopy growth precedes senescence in 2005 and 2010 Amazonian droughts. *Remote Sens. Environ.* **211**, 26–37 (2018).
17. Vancutsem, C. *et al.,* Long-term (1990–2019) monitoring of forest cover changes in the humid tropics. *Sci. Adv.* **7**, eabe1603 (2021).
18. Steele-Dunne, S. C., Friesen, J., Van de Giesen, N. Using diurnal variation in backscatter to detect vegetation water stress. *IEEE Trans. Geosci. Remote Sens.* **50**, 2618–2629 (2012).
19. Guan, K. *et al.,* Seasonal coupling of canopy structure and function in African tropical forests and its environmental controls, *Ecosphere* **4**, 1–21 (2013).
20. Konings, A. G. *et al.,* Active microwave observations of diurnal and seasonal variations of canopy water content across the humid African tropical forests. *Geophys. Res. Lett.* **44**, 2290–2299 (2017).
21. Tropical Rainfall Measuring Mission (TRMM) (2011), TRMM (TMPA/3B43) Rainfall Estimate L3 1 month 0.25 degree x 0.25 degree V7, Greenbelt, MD, Goddard Earth Sciences Data and Information Services Center (GES DISC), Accessed: [5.10. 2019], 10.5067/TRMM/TMPA/MONTH/7
22. Sankaran, M. *et al.,* Determinants of woody cover in African savannas. *Nature* **438**, 846–849 (2005).
23. Phillips, O. L. *et al.,* Drought sensitivity of the Amazon rainforest. *Science* **323**, 1344–1347 (2009).
24. Aragão, L. E. O. *et al.,* Spatial patterns and fire response of recent Amazonian droughts. *Geophys. Res. Lett.* **34**, L07701 (2007).
25. Funk, C. *et al.,* The climate hazards infrared precipitation with stations—a new environmental record for monitoring extremes. *Sci. Data* **2**, 150066 (2015).
26. Martens, B. *et al.,* GLEAM v3: satellite-based land evaporation and root-zone soil moisture. *Geosci. Model Dev.* **10**, 1903–1925 (2017).
27. Saatchi, S. S. *et al.,* Persistent effects of a severe drought on Amazonian forest canopy. *Proc. Natl. Acad. Sci. USA* **110**, 565–570 (2013).
28. Verbesselt, J. *et al.,* Detecting Trend and Seasonal Changes in Satellite Image Time Series. *Remote Sens. Environ* **114**, 106–115 (2010).

29. Wan, Z. New refinements and validation of the MODIS land-surface temperature/emissivity products. *Remote Sens. Environ.* **112**, 59–74 (2008).
30. Muñoz Sabater, J., (2021): ERA5-Land monthly averaged data from 1950 to 1980. Copernicus Climate Change Service (C3S) Climate Data Store (CDS). (Accessed on < 11-11-2021 >), 10.24381/cds.68d2bb3
31. Scheffer, M. *et al.,* Early-warning signals for critical transitions. *Nature* **461**, 53–59 (2009).
32. Verbesselt, J. *et al.,* Remotely sensed resilience of tropical forests. *Nat. Clim. Change* **6**, 1028–1031 (2016).
33. Lloret, F., Keeling, E. G., Sala, A. Components of tree resilience: effects of successive low-growth episodes in old ponderosa pine forests. *Oikos* **120**, 1909–1920 (2011).
34. Phillips, O. L. *et al.,* Drought–mortality relationships for tropical forests. *New Phytol*. **187**, 631–646 (2010).
35. Kendall, M.G. Rank correlation methods, 4th ed. Charles Griffin, London (1975).
36. Lehmann, E. L., Nonparametrics: Statistical Methods Based on Ranks, Holden-Day, San Francisco, California, USA (1975).
37. van der Schrier G, Barichivich J, Briffa KR and Jones PD (2013) A scPDSI-based global data set of dry and wet spells for 1901-2009. J. Geophys. Res. Atmos. 118, 4025-4048 (10.1002/jgrd.50355).
38. Hansen, M. C. *et al.,* High-resolution global maps of 21st-century forest cover change. *Science* **342**, 850–853 (2013).
39. Grantham, H. S. *et al.,* Anthropogenic modification of forests means only 40% of remaining forests have high ecosystem integrity. *Nat. Commun.* **11**, 5978 (2020).
40. Wigneron, J. P. *et al.,* Tropical forests did not recover from the strong 2015–2016 El Niño event. *Sci. Adv.* **6**, eaay4603 (2020).
41. Tropical Rainfall Measuring Mission (TRMM) (2011), TRMM (TMPA) Rainfall Estimate L3 3 hour 0.25 degree x 0.25 degree V7, Greenbelt, MD, Goddard Earth Sciences Data and Information Services Center (GES DISC), Accessed: [15.12. 2021], 10.5067/TRMM/TMPA/3H/7
42. Fu, R. *et al.,* Increased dry-season length over southern Amazonia in recent decades and its implication for future climate projection. *Proc. Natl. Acad. Sci. USA* **110**, 18110–18115 (2013).
43. Jiang, Y. *et al.,* Widespread increase of boreal summer dry season length over the Congo

rainforest. *Nat. Clim. Change* **9**, 617–622 (2019).

44. Ziese, M. *et al.,* GPCC Full Data Daily Version. 2018 at 1.0°: Daily Land-Surface Precipitation from Rain-Gauges built on GTS-based and Historic Data. (2018). doi: 10.5676/DWD_GPCC/FD_D_V2018_100.
45. Xu, X. *et al.,* Leaf surface water, not plant water stress, drives diurnal variation in tropical forest canopy water content. *New Phytol.* **231**,122–136 (2021).
46. Bartlett, M. K., *et al.,* The correlations and sequence of plant stomatal, hydraulic, and wilting responses to drought. *PNAS* **113**, 13098–13103 (2016).
47. Tucker, C. J. *et al.,* An extended AVHRR-8km NDVI dataset compatible with MODIS and SPOT vegetation NDVI data. *Int. J. Remote Sens.* **26**, 4485–4498 (2005).
48. Pinzon, J. E., Tucker, C. J. A Non-Stationary 1981-2012 AVHRR NDVI3g Time Series. *Remote Sens.* **6**, 6929–6960 (2014).
49. Zhu, Z. *et al.,* Global data sets of vegetation leaf area index (LAI) 3g and fraction of photosynthetically active radiation (FPAR) 3g derived from global inventory modeling and mapping studies (GIMMS) normalized difference vegetation index (NDVI3g) for the period 1981 to 2011. *Remote Sens.* **5**, 927–948 (2013).
50. Liu, Y., Liu, R., Chen, J. M. Retrospective retrieval of long‐term consistent global leaf area index (1981–2011) from combined AVHRR and MODIS data. *J. Geophys. Res. Biogeosci.* 117, (G4) (2012).
51. Chen, C. *et al.,* China and India lead in greening of the world through land-use management. *Nat. Sustain.* **2**, 122–129 (2019).
52. Leitold, V. *et al.,* El Niño drought increased canopy turnover in Amazon forests. *New Phytol*. **219**, 959–971 (2018).
53. Aleixo, I. *et al.,* Amazonian rainforest tree mortality driven by climate and functional traits. *Nat. Clim. Change* **9**, 384–388 (2019).
54. Liu, Y. Y. *et al.,* Recent reversal in loss of global terrestrial biomass. *Nat. Clim. Change* **5**, 470–474 (2015).
55. Xu, L. *et al.,* Changes in global terrestrial live biomass over the 21st century. *Sci. Adv.* **7**, eabe9829 (2021).
56. Feldpausch, T. R. *et al.,* Amazon forest response to repeated droughts. *Global Biogeochem. Cycles* **30**, 964–982 (2016).

57. Warton, D. I., Duursma, R. A., Falster, D. S., Taskinen, S. smatr 3 - an R package for estimation and inference about allometric lines. *Methods Ecol. Evol.* **3**, 257–259 (2012).

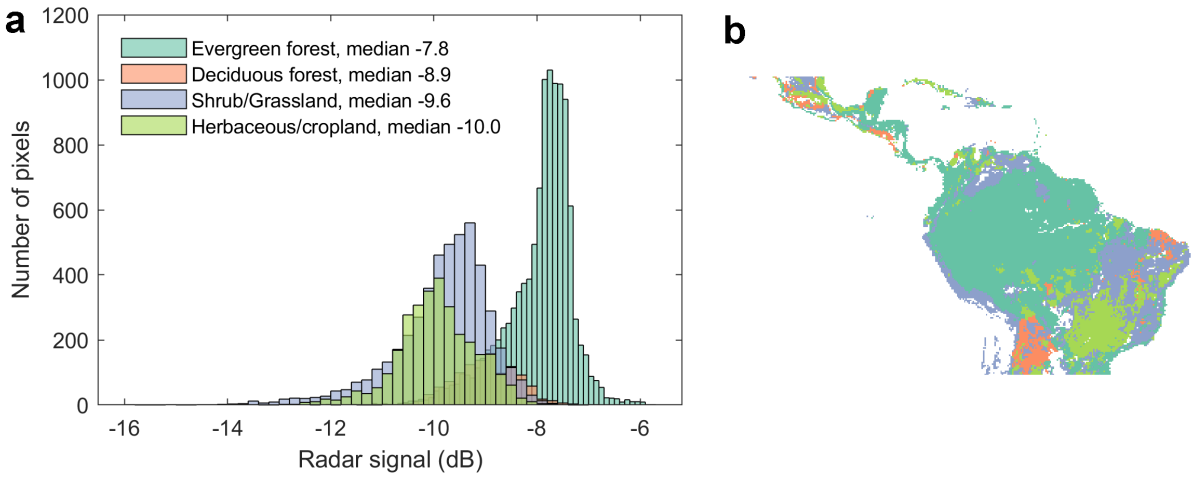

Fig. S1. (a) Histograms of the C-band ASCAT signal (in unit of dB, monthly averaged between 2007 and 2018) for four land-cover types in part of the Neotropics. **(b)** shows the spatial distribution of the four types of land-cover. Land cover information was taken from the European Space Agency (ESA) Climate Change Initiative (CCI) land-cover map for the year 2015 (maps.elie.ucl.ac.be/CCI/viewer/).

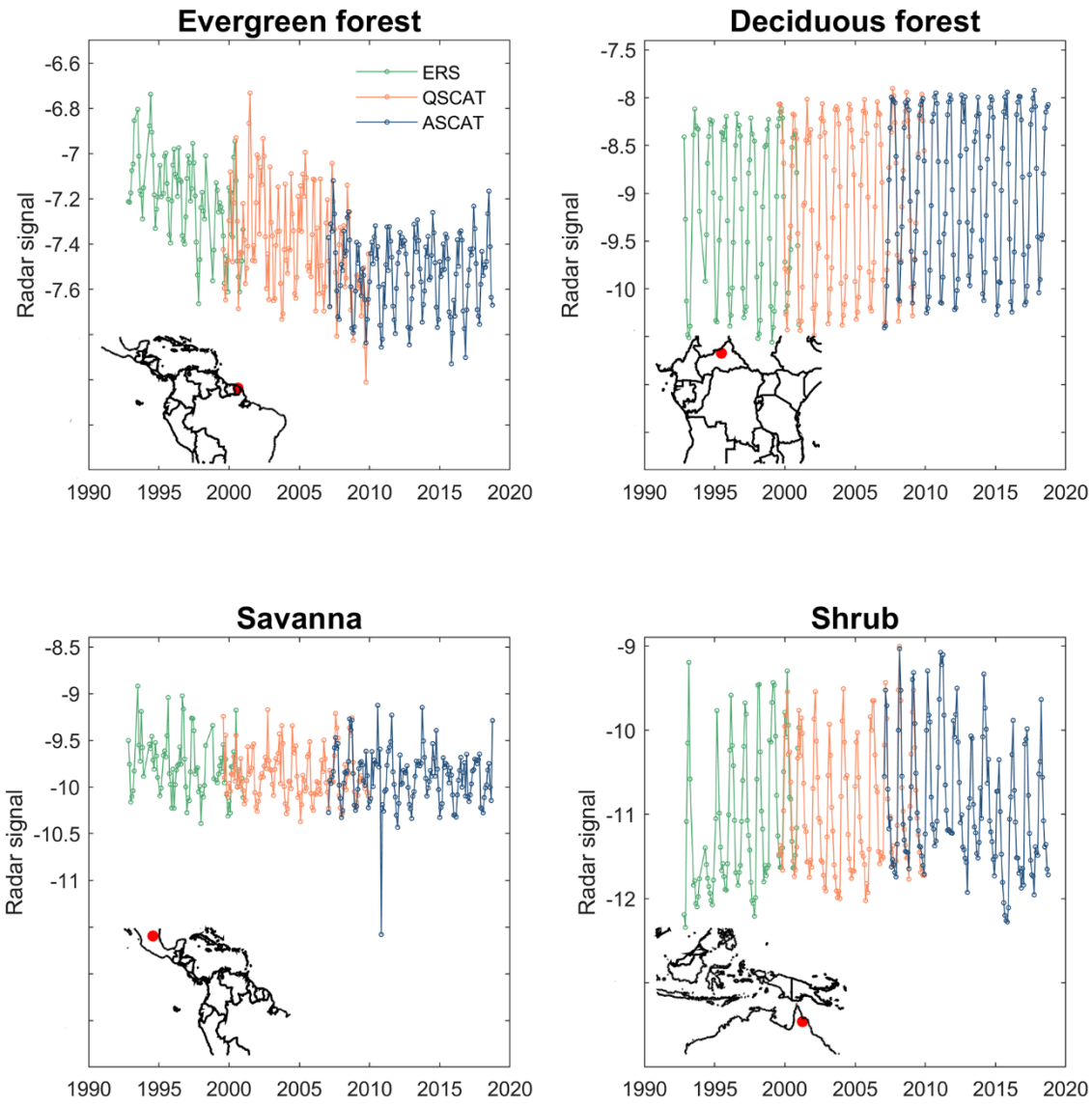

Fig. S2. Merged radar data in different land-cover types. Each panel shows the time series of the merged radar signal over one 25 km pixel. The position of the pixel is displayed as a red dot in the lower-left part of each panel.

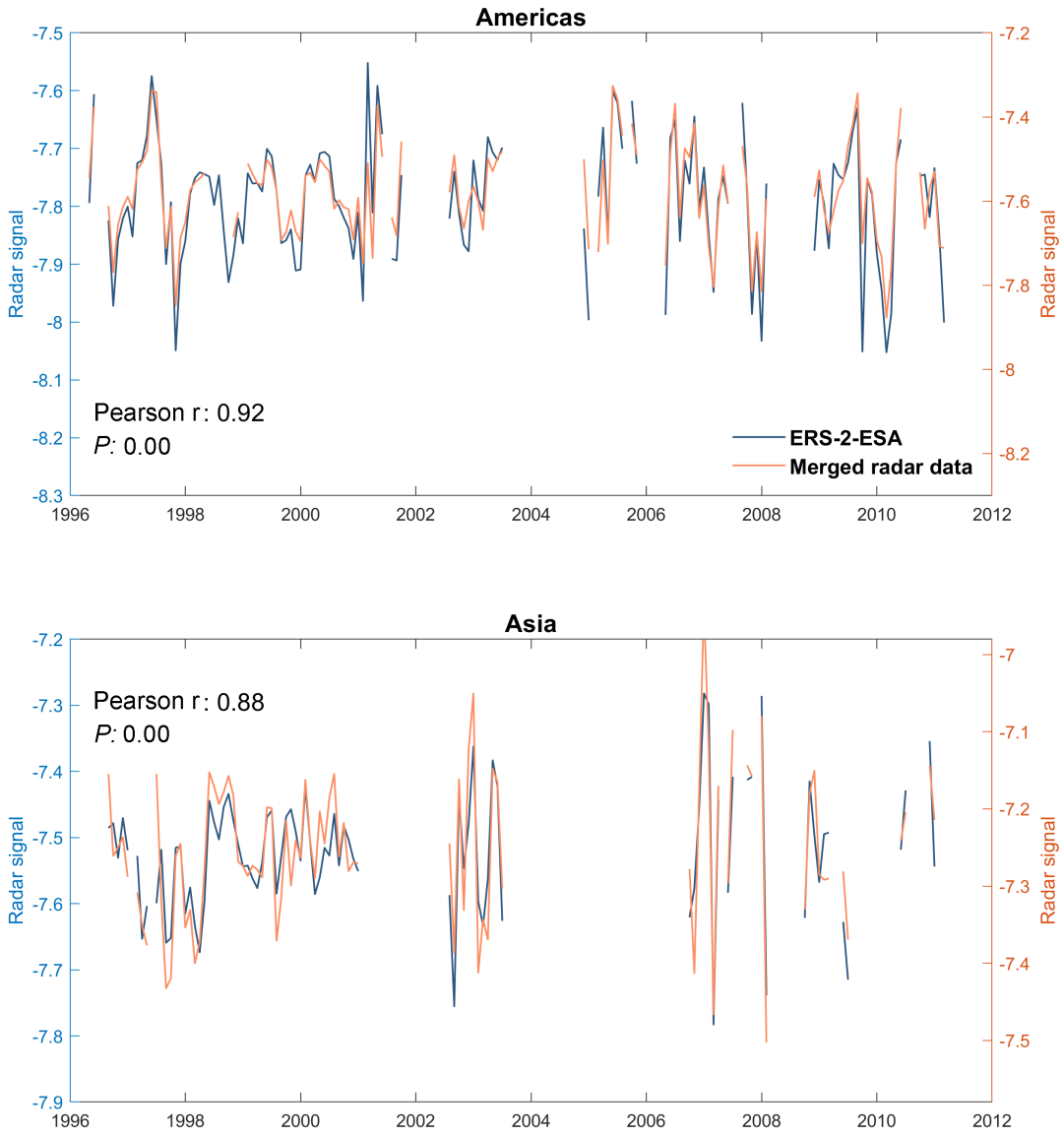

Fig. S3. Validation of merged radar data against ERS-2-ESA data. The orange line represents the radar data set used in the present study. It was compared with the ERS-2-ESA data set at a subset of pixels sampled by the ERS-2 satellite. The correlation between the two timeseries is high, both in the Americas and in Asia.

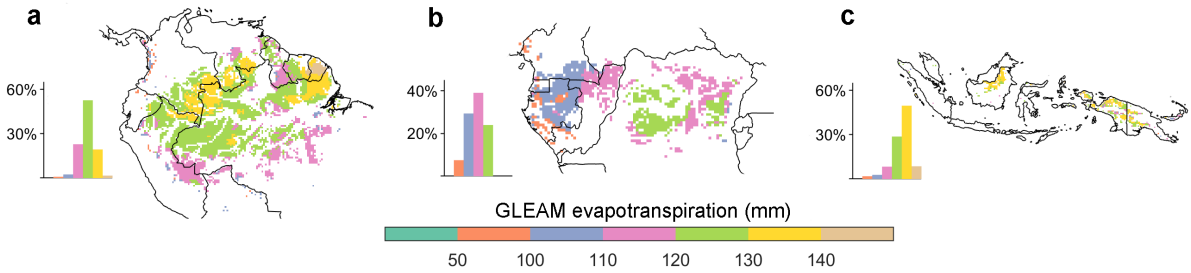

Fig. S4. Spatial patterns of GLEAM month evapotranspiration, averaged across all months in 1992–2018. The histograms beside each regional map show the proportion of pixels in each evapotranspiration class. The colour scheme is the same in the histograms and maps.

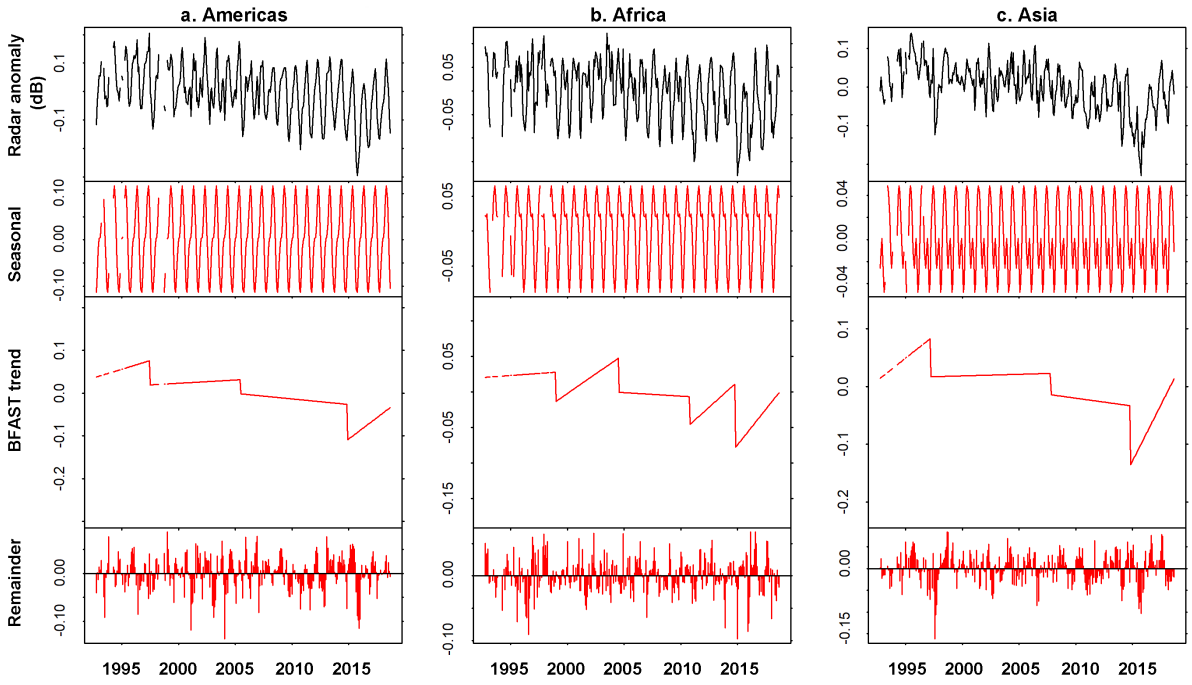

Fig. S5. BFAST (Breaks for Additive Season and Trend algorithm) decomposition of the radar signal. The monthly radar anomalies (averaged across all pixels within a continent) are presented in the upper panel, followed by the estimated seasonal amplitude, the "breaks" in radar signal detected by BFAST, and finally the remainder (the variation of the signal after removing the trend).

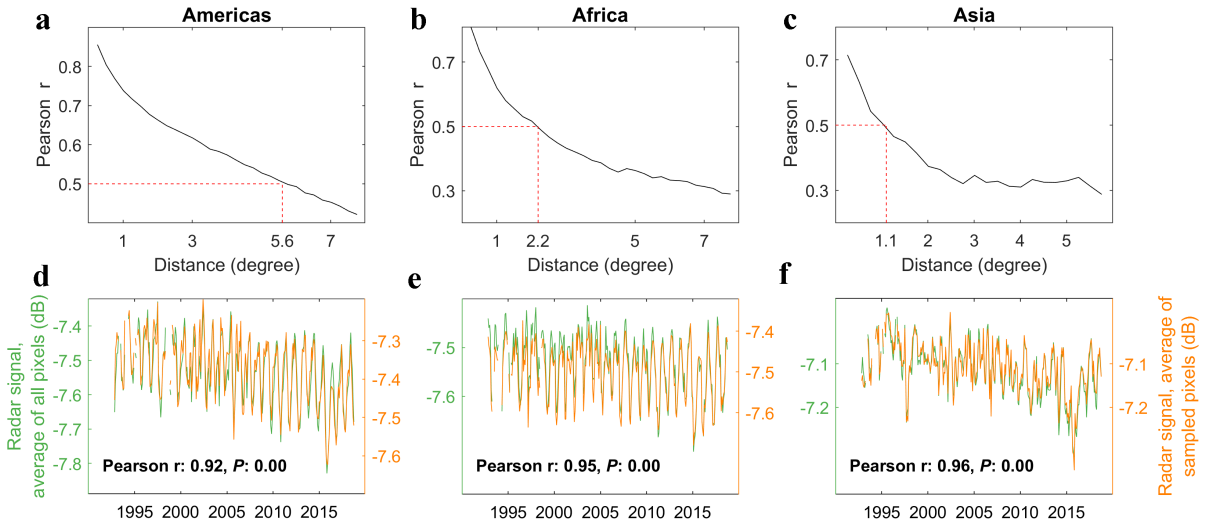

Fig. S6. Influence of spatial autocorrelation on the radar signal trends. (a-c) show the decrease in radar signal correlation as a function of distance between pixel pairs. The distance is calculated on the basis of the latitudes and longitudes of the pixel centers, and therefore has a unit of degree which is about 110 kilometers at the equator. A distance D2 corresponding to a Pearson r of 0.5 was identified, which was 5.6 degrees in tropical Americas, 2.2 degrees in Africa, and 1.1 degrees in Asia. (d-f) show the time series of radar signal as in Fig. 1 of the main text (in green) or calculated as average across pixels greater than the D2 distance (in orange).

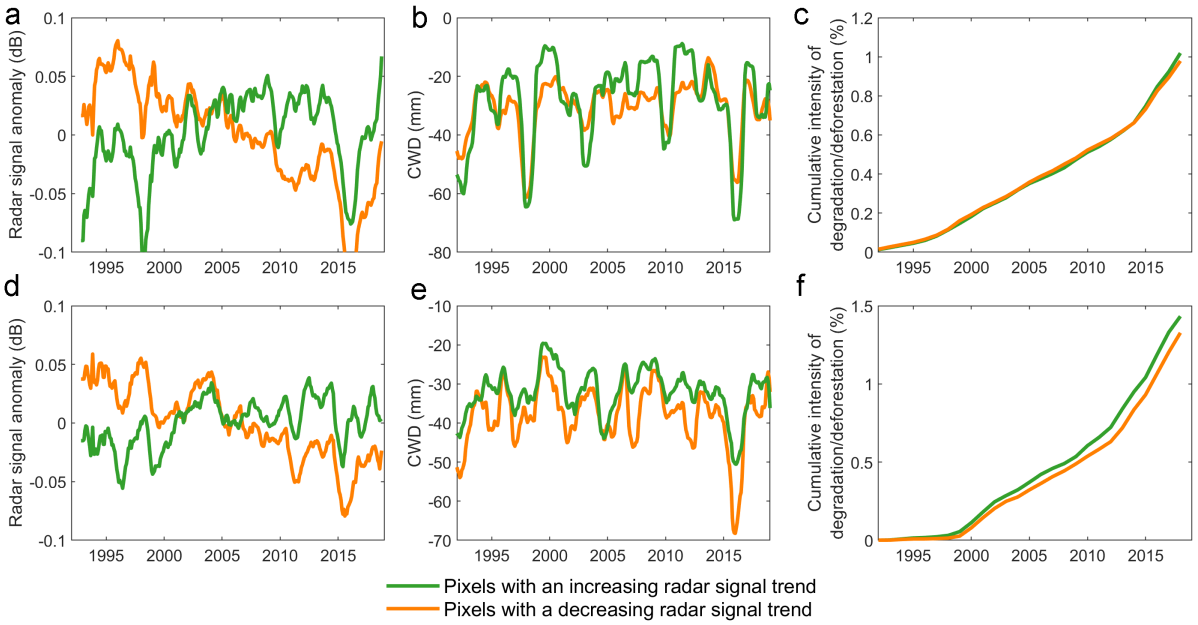

Fig. S7. Time series of radar signal anomaly, cumulative water deficit (CWD), and cumulative forest degradation/deforestation intensity, for two types of rainforests in tropical Americas (a-c) and Africa (d-f). Pixels with an increasing radar signal trend (colored in green), were compared to pixels with a decreasing trend (colored in orange). See Fig. 2a & 2b in the main text for the spatial distributions of the pixels. The time series shown in (a), (b), (d) and (f) are 12-month moving averages. Panels (c) and (f) show the cumulative intensity of degradation/deforestation, calculated as the cumulative area of the 30 m resolution degraded/deforested forest pixels, divided by the total area of all the radar pixels with an increasing (colored in green) or a decreasing (colored in orange) signal trend.

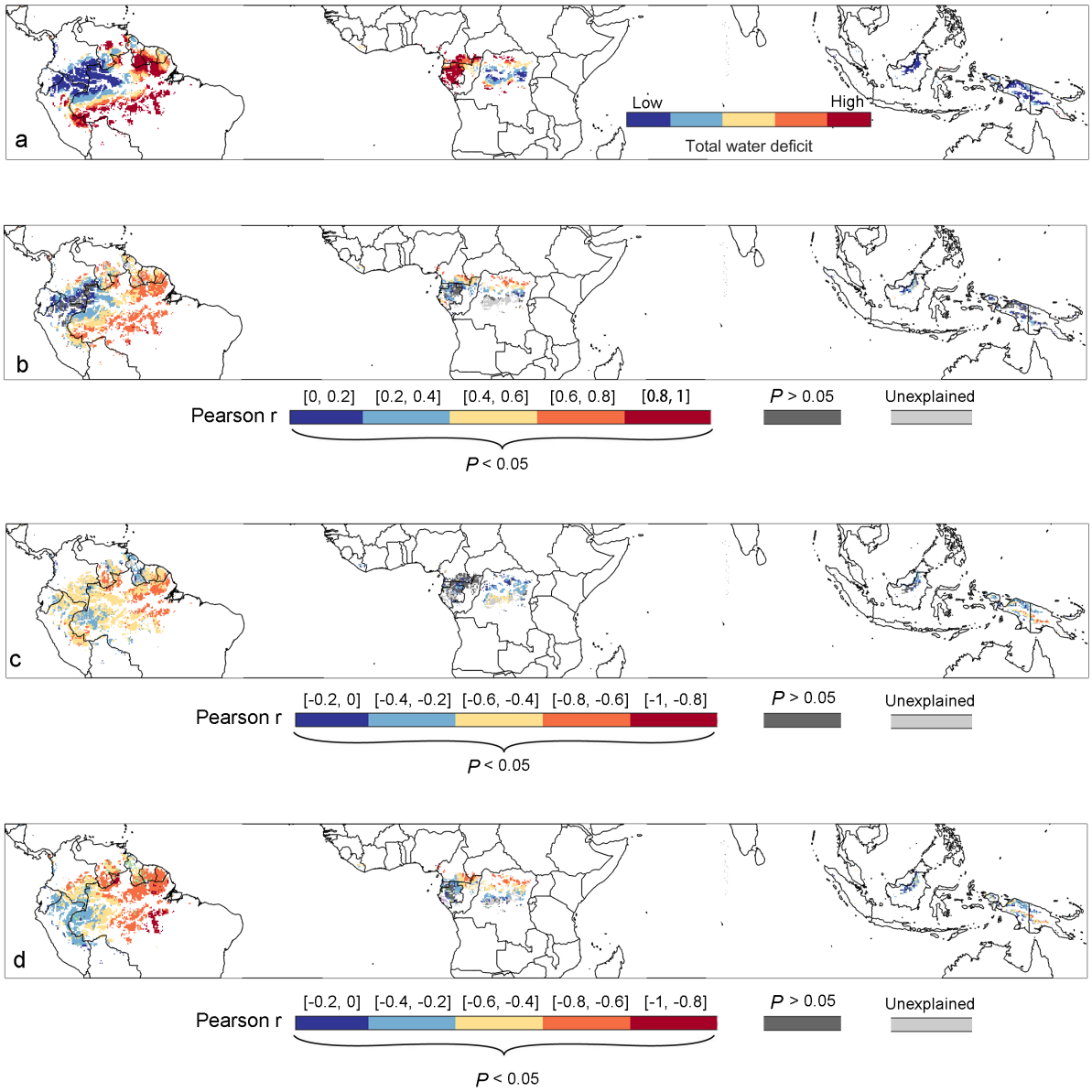

Fig. S8. Spatial pattern of total water deficit between 1992 and 2018 (a), and correlations (Pearson *r*) between radar time series and (b) cumulative water deficit, (c) MODIS daytime land surface temperature, and (d) ERA5 monthly mean air temperature. The total water deficit in (**a**) was calculated as the sum of all monthly cumulative water deficits between 1992 and 2018. In (b-d), regions with increased radar signals were coloured light gray ('Unexplained') and were explored independently (Fig. S7).

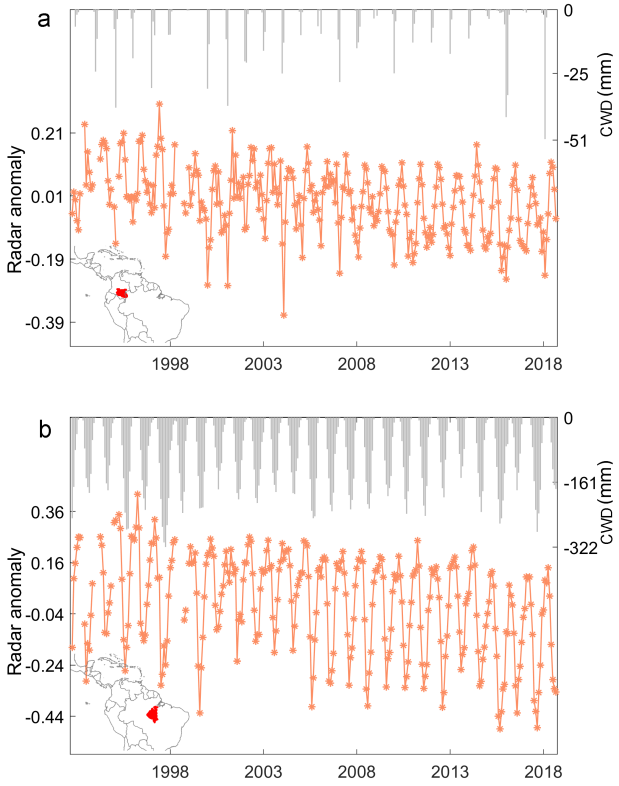

Fig. S9. Radar signal and cumulative water deficit (CWD) in two typical forest regions. (a) Caqueta moist forests in northwestern Amazonia. (b) Tapajós-Xingu moist forests in southern Amazonia. CWD values were generally close to zero in (**a**), in contrast to those in (**b**). However, in the rare cases of water deficit in (**a**), the radar signal still decreased.

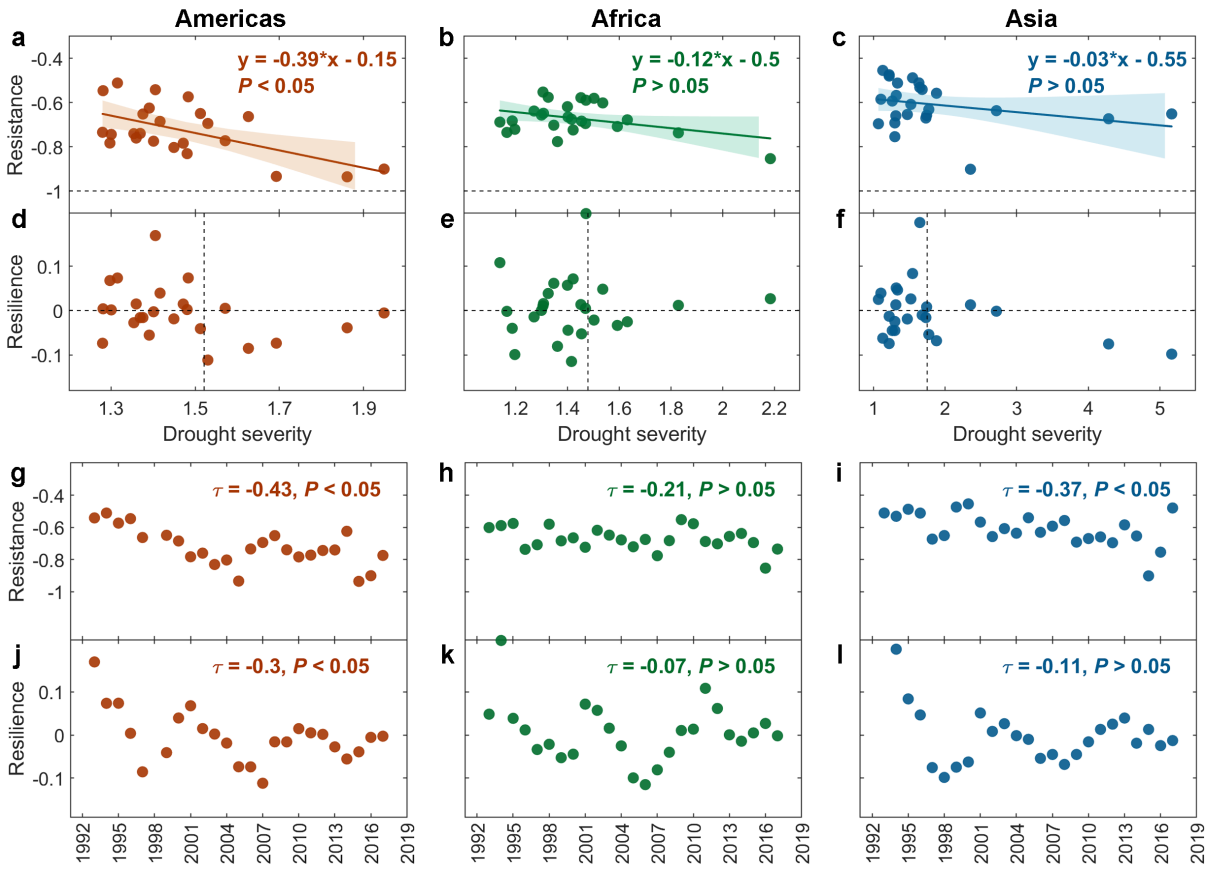

Fig. S10. Drought resistance and resilience calculated with a three-year drought legacy length. a-f show the drought resistance and resilience as a function of drought severity for intact tropical rainforests in three continents. g-l show the time series of drought resistance and resilience. The notations are the same as those described in the legends to Figs. 3 & 4 in the main text.

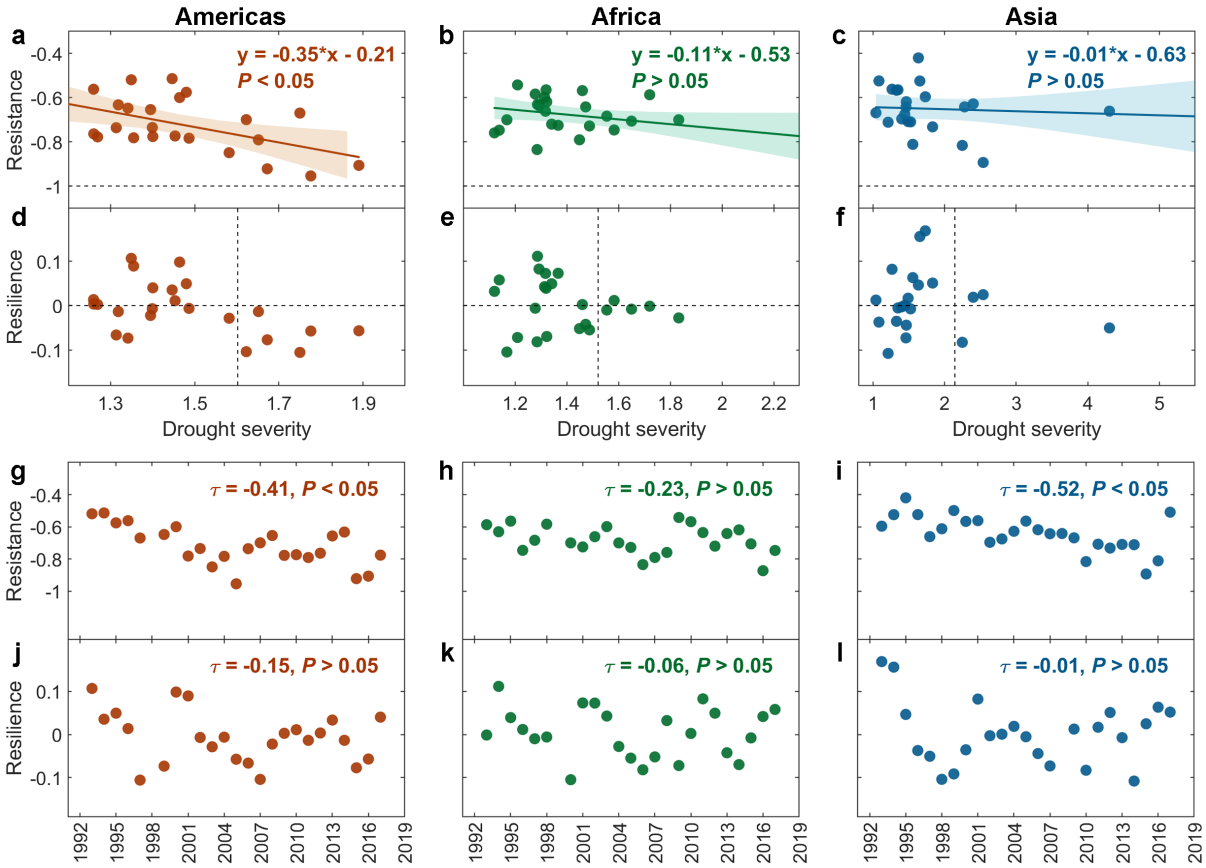

Fig. S11. Drought resistance and resilience calculated with droughts defined by Z-score of MCWD but assuming a monthly evapotranspiration of 100 mm for calculating MCWD. a-f show the drought resistance and resilience as a function of drought severity for intact tropical rainforests in three continents. g-l show the time series of drought resistance and resilience. The notations are the same as those described in the legends to Figs. 3 & 4 in the main text.

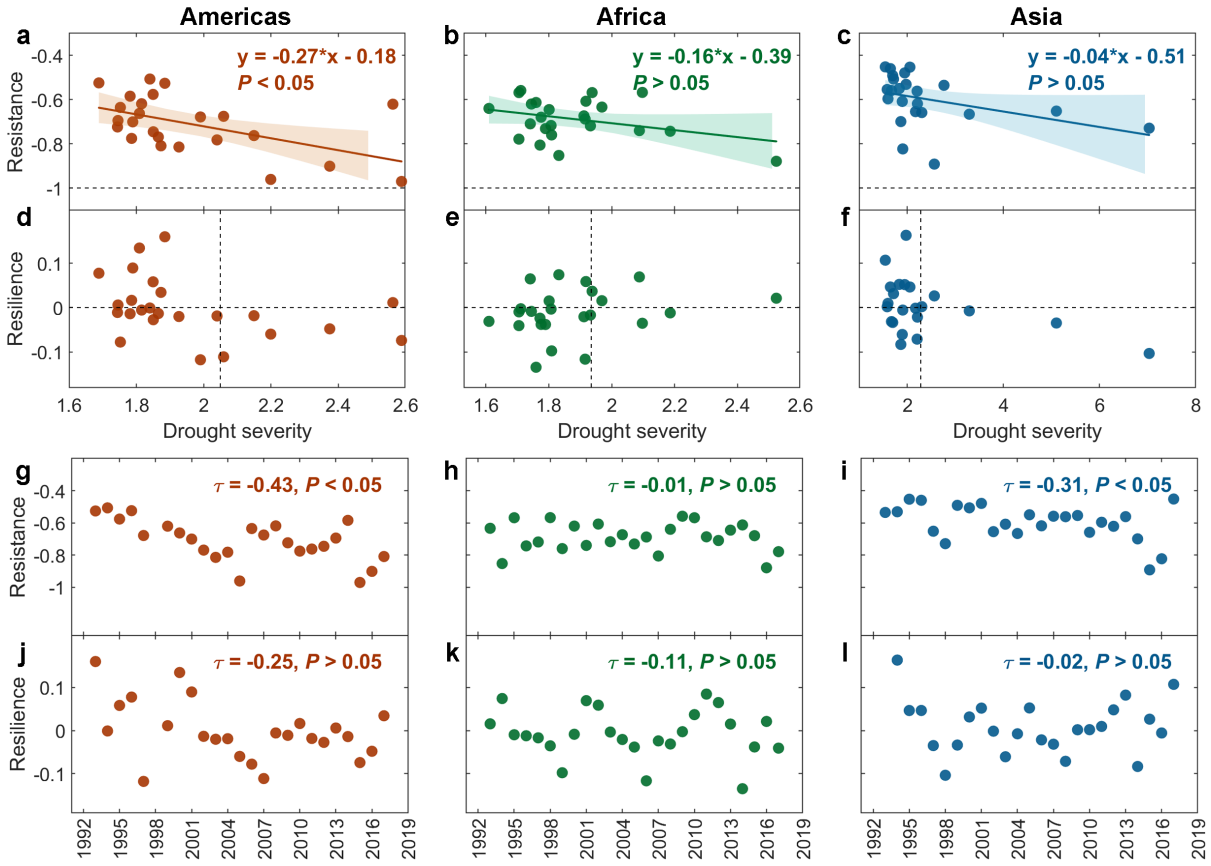

Fig. S12. Drought resistance and resilience calculated with a threshold of -1.5 for Z-score of MCWD for defining droughts. a-f show the drought resistance and resilience as a function of drought severity for intact tropical rainforests in three continents. g-l show the time series of drought resistance and resilience. The notations are the same as those described in the legends to Figs. 3 & 4 in the main text.

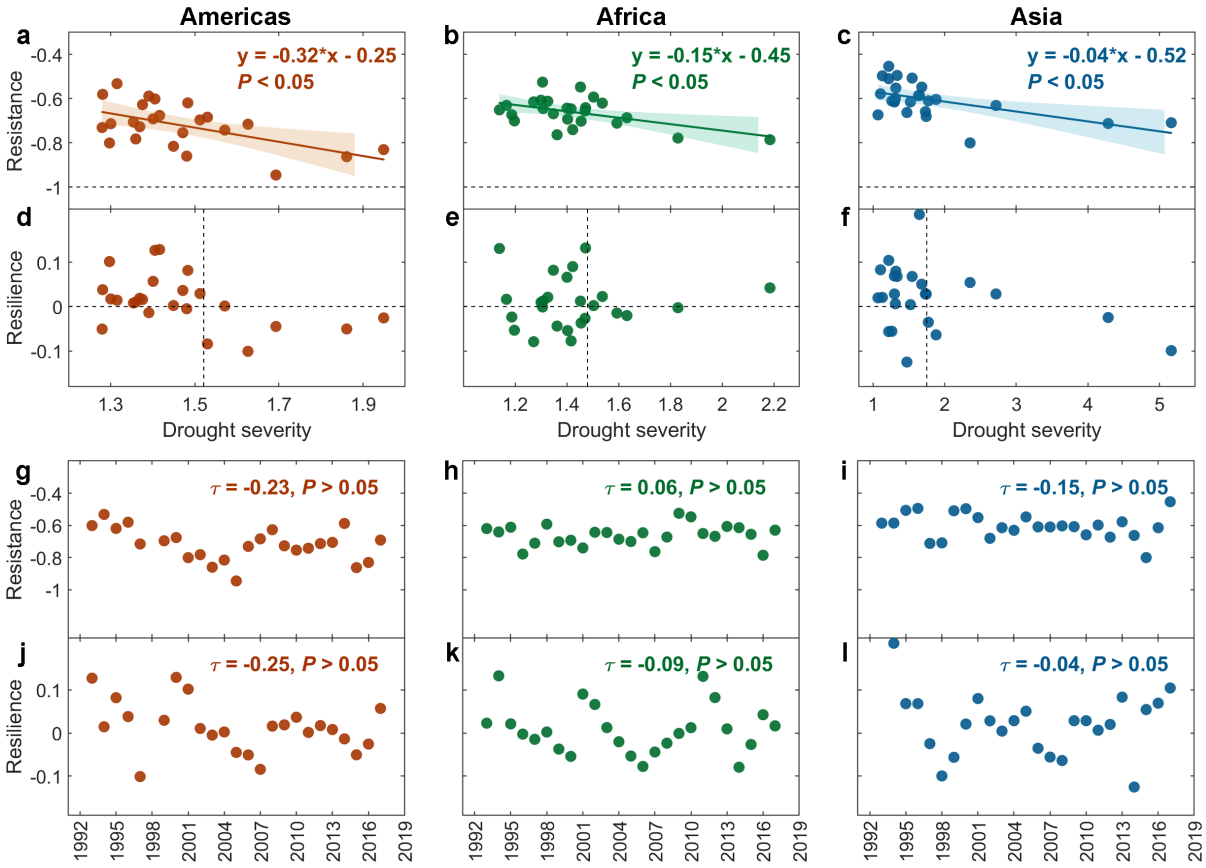

Fig. S13. Drought resistance and resilience calculated after detrending the radar signal. a-f show the drought resistance and resilience as a function of drought severity for intact tropical rainforests in three continents. g-l show the time series of drought resistance and resilience. The notations are the same as those described in the legends to Figs. 3 & 4 in the main text.

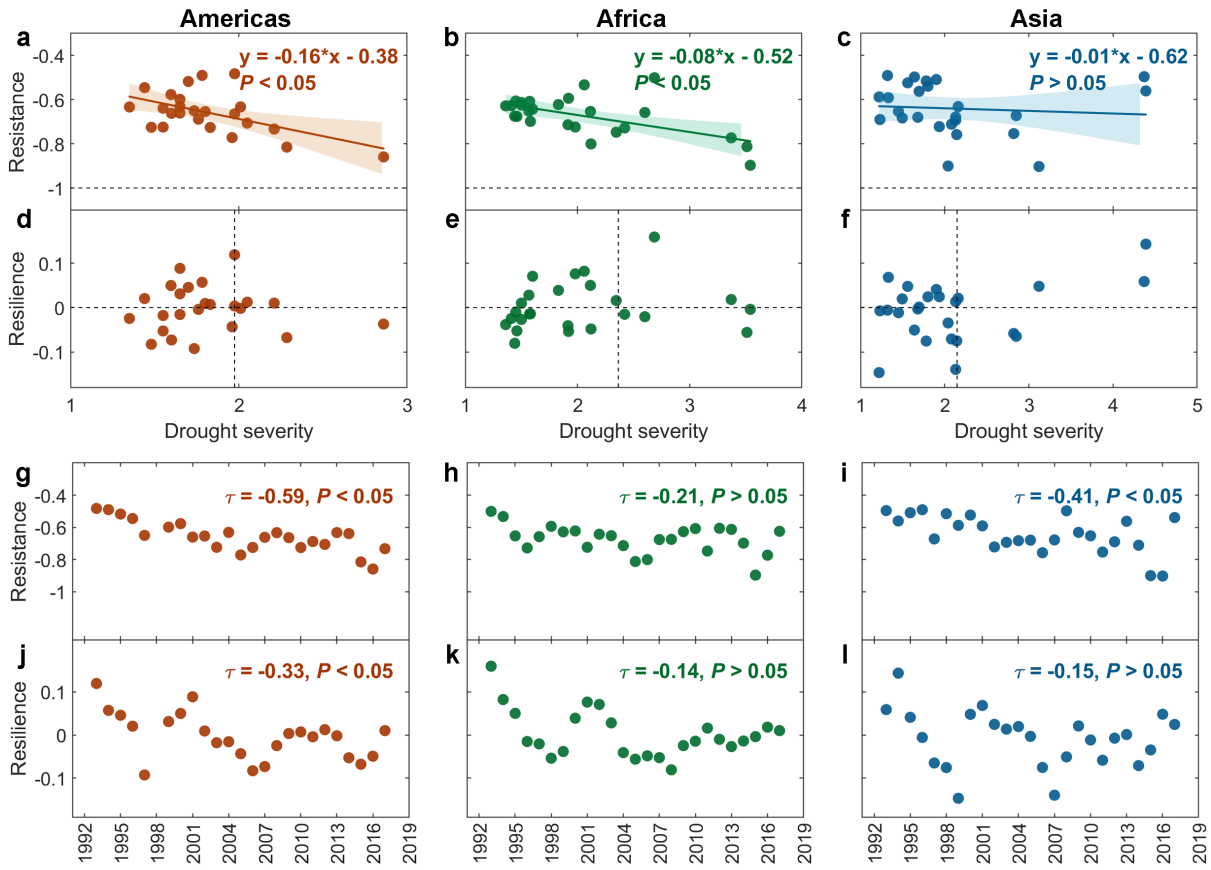

Fig. S14. Drought resistance and resilience calculated with droughts defined by CRU scPDSI. a-f show the drought resistance and resilience as a function of drought severity for intact tropical rainforests in three continents. g-l show the time series of drought resistance and resilience. A threshold of -1 was applied on scPDSI to define past droughts. The absolute value of scPDSI was used to indicate the drought severity. Other notations are the same as those described in the legends to Figs. 3 & 4 in the main text.

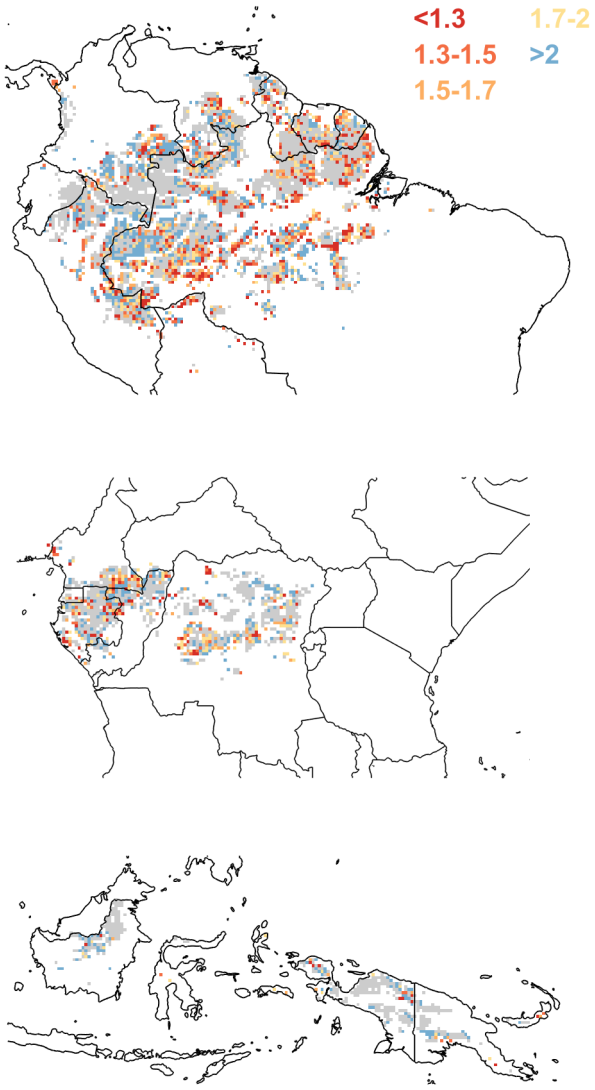

Fig. S15. Spatial pattern of the drought severity threshold beyond which the forest cannot recover its pre-drought state. Pixels coloured in gray are forests where such threshold was not detected. Drought severity was calculated as the absolute value of the Z-score of maximum cumulative water deficit within a year (MCWD). The drought severity threshold was such that above the threshold all estimated resilience values were negative.

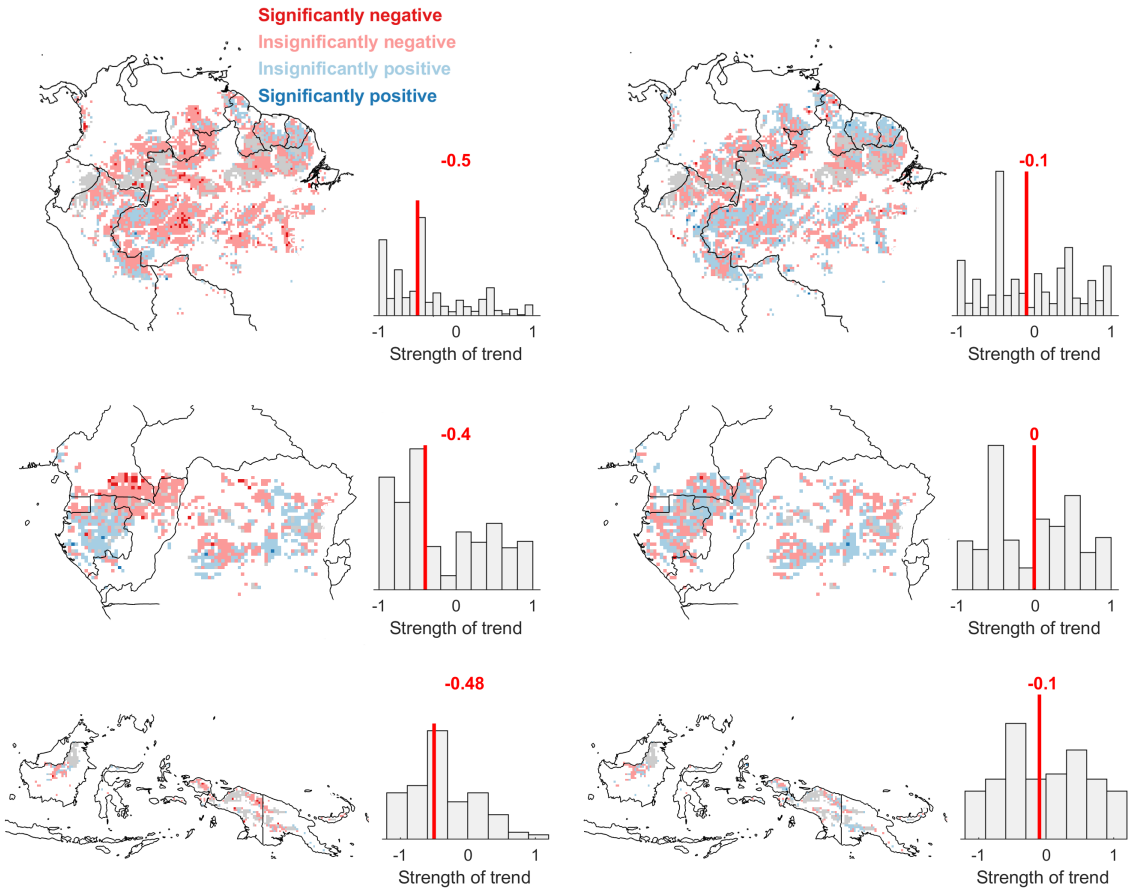

Fig. S16. Temporal trends in drought resistance (a-c) and resilience (d-f) for intact tropical rainforests. Trends were tested using Spearman's rho test. Negative values (warm colours) mean decreasing trends, and positive values (cool colours) mean increasing trends, with their absolute value representing the strength of the trend. Trends with a P value < 0.05 were deemed as significant. The histogram shows the distribution of trend strengths across all pixels, with the median value marked and labelled in red. Pixels coloured in gray are forests where less than two droughts occurred, so where no trend is available.

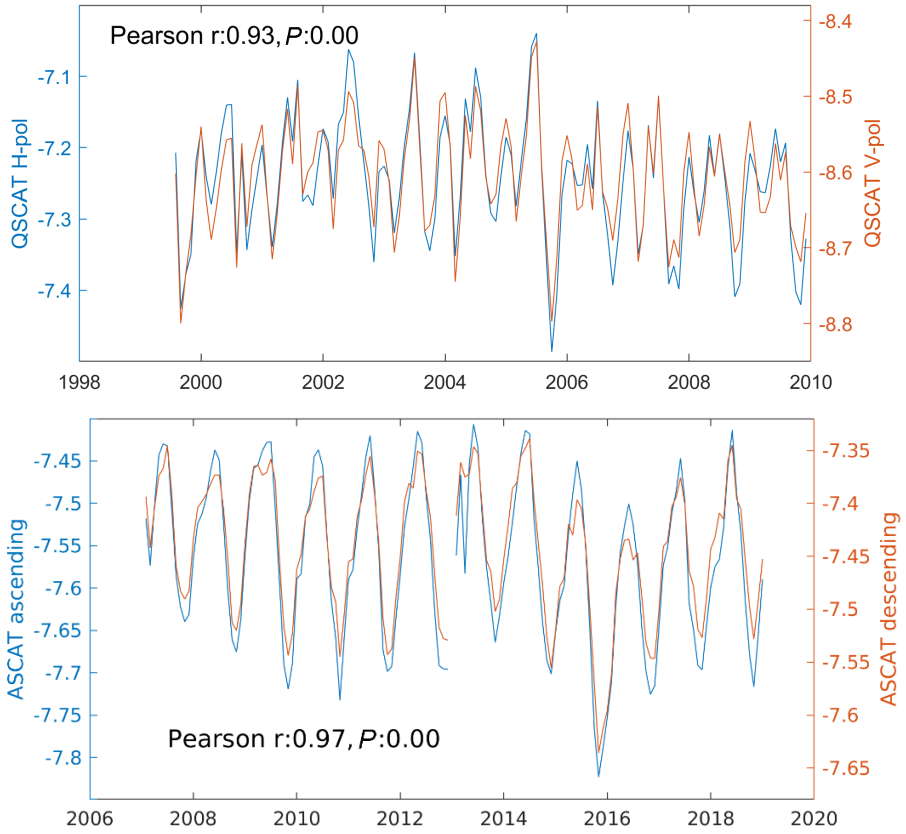

Fig. S17. Effect of polarisation and the choice of the ascending versus descending paths on the radar signal. (Top) Comparison of monthly mean QSCAT signals from V-polarization and H-polarization modes over Amazonian intact rainforests. (Bottom) Comparison of monthly mean ASCAT signals from ascending and descending paths over Amazonian intact rainforests.

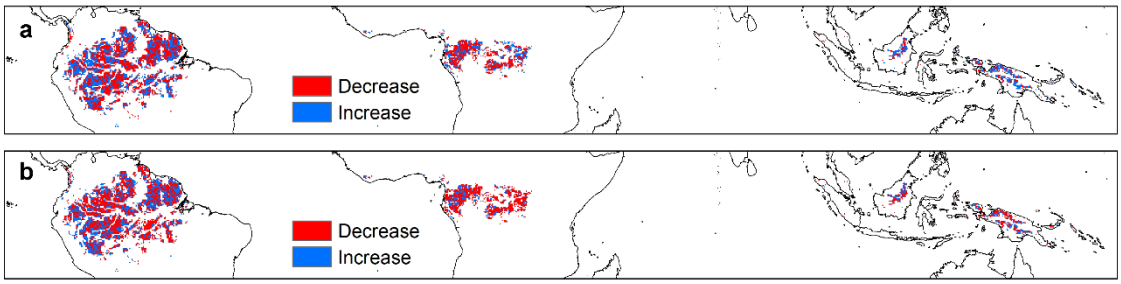

Fig. S18. Spatial pattern of the temporal trends in rain rate (>5 mm/hour) observed at the time of the QSCAT acquisition (**a**, 6:00 am of each day in 1999-2009) and ASCAT acquisition (**b**, 21:30 pm of each day in 2007-2018).

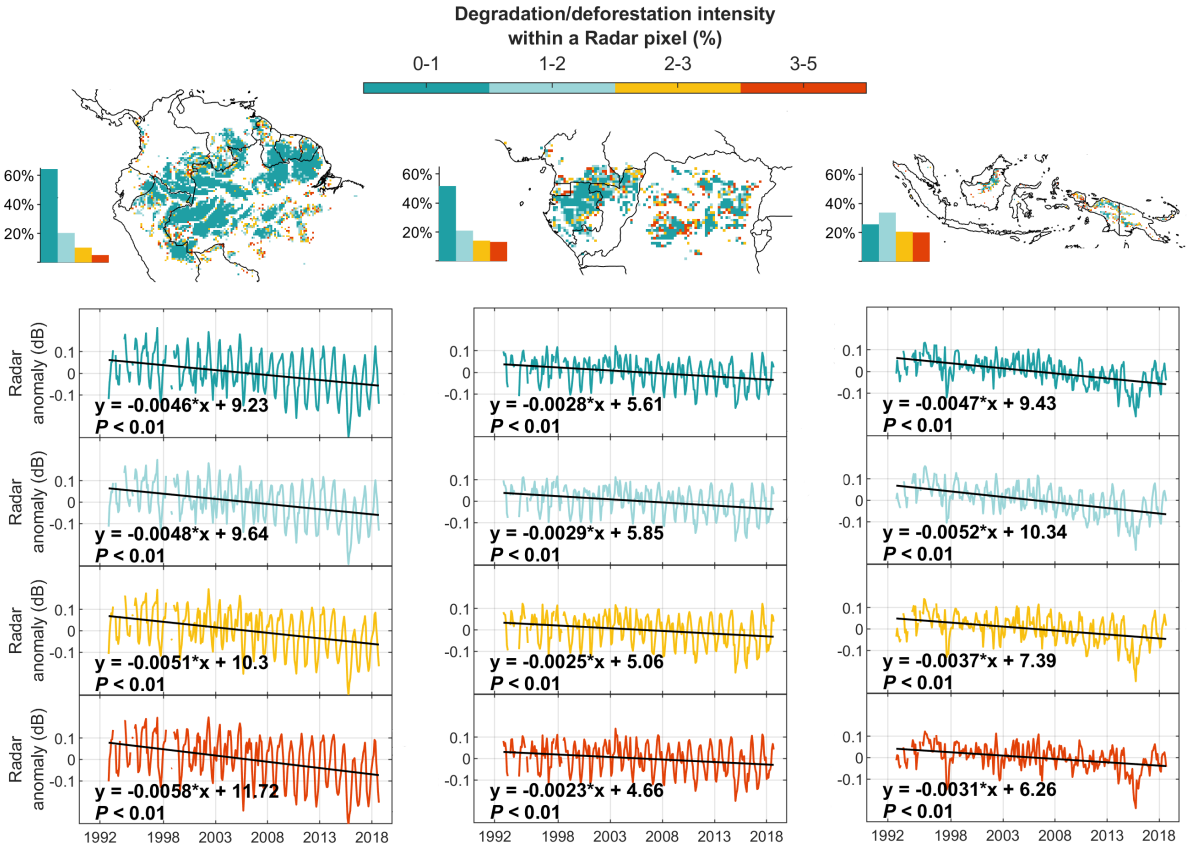

Fig. S19. Spatial patterns and radar signals for intact tropical rainforest pixels categorized into four groups of degradation/deforestation intensity. The shown intact tropical rainforest pixels were defined using the 2020 baseline map of undisturbed tropical forests provided by Vancutsem et al. (*17*, See Section 4). For each pixel, its degradation/deforestation intensity was calculated as the total area of all the 30 m forest pixels that were either degraded or deforested during 1992 -2018, divided by the radar pixel area (25 × 25 km). For each pixel group, anomalies of the averaged radar signals were plotted. A trend line was fitted to the anomalies, and the regression and *P* value were provided.

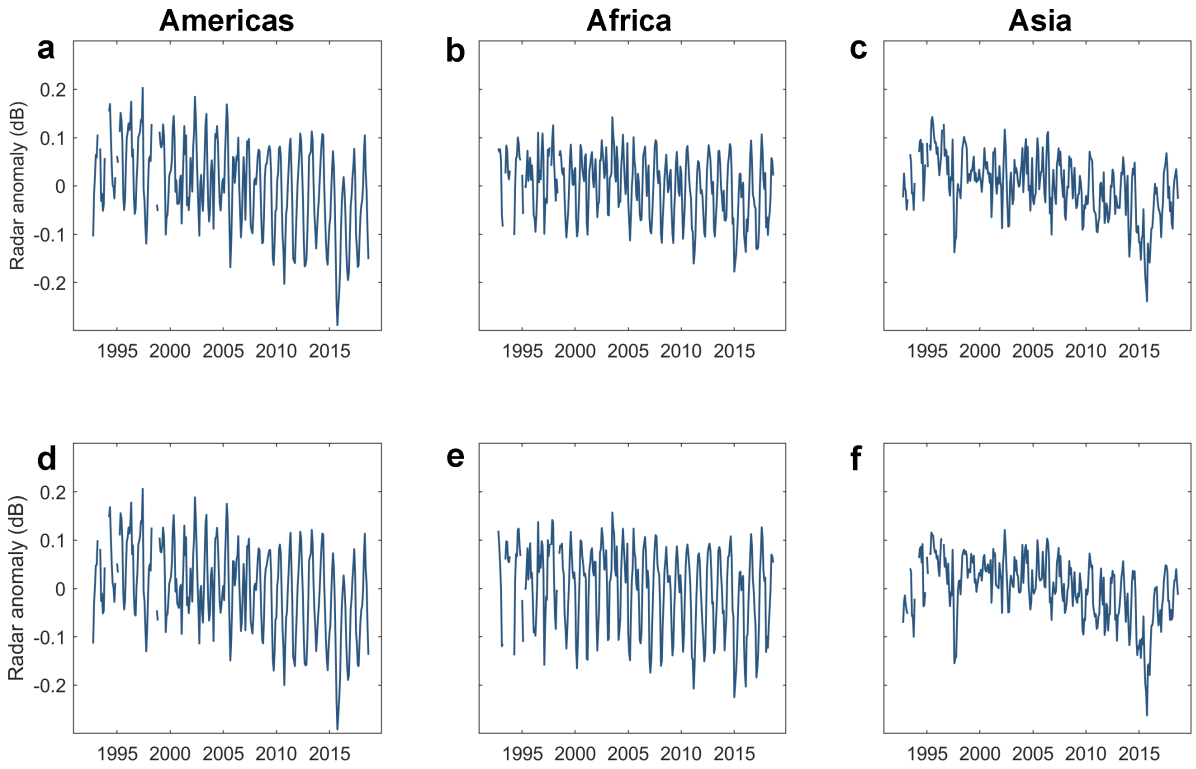

Fig. S20. Radar signals averaged across intact rainforest pixels defined by (a-c) the Hansen forest cover change maps and (d-f) the Forest Integrity Index map. This figure demonstrates that the results reported in Fig. 1 in the main text do not strongly depend on the definitions of intact rainforest pixels. Please see the last paragraph of Section 12 for more details on these alternative definitions of intact rainforest pixels.

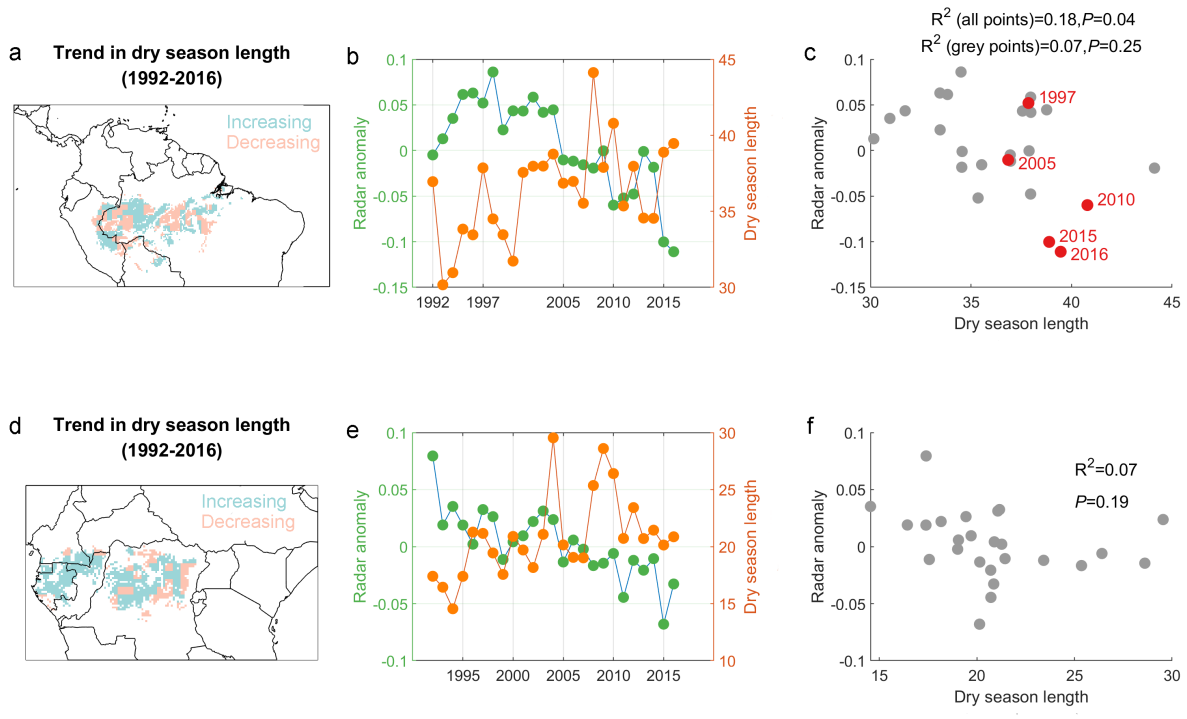

Fig. S21. Dry season length as a function of radar signals for southern Amazonia (a-c) and central Africa (d-f). The unit of the dry season length is pentad (5 days), and the unit of radar signal anomaly is decibel (dB). The length of the dry season was correlated with the decrease in the annual radar signal in southern Amazonia, although with a low correlation coefficient (R^2=0.18). This effect was attributed to the increased frequency of severe droughts during the study period.

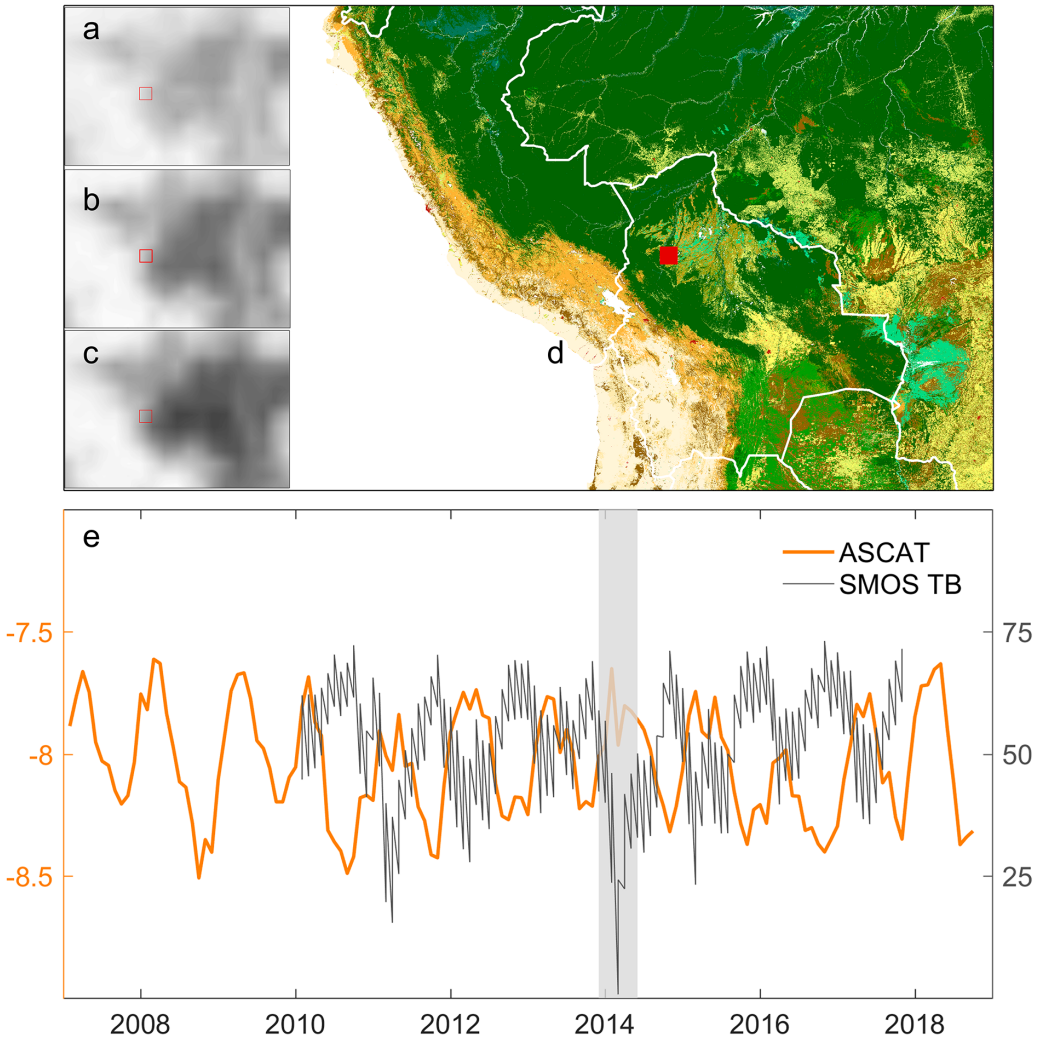

Fig. S22. ASCAT backscatter and SMOS brightness temperature (TB) during a severe flood in February 2014 in southwestern Amazonia. The progression of this flood was captured by SMOS brightness temperature images in (**a**) December 2013, (**b**) January 2014, and (**c**) February 2014. The red rectangle shows the location of a forest that was flooded (**a–d**). The ASCAT and SMOS TB signals of this forest were shown in (**e**). European Space Agency (ESA) Climate Change Initiative (CCI) land-cover map for the year 2015 (maps.elie.ucl.ac.be/CCI/viewer/) was used as background in (**d**).

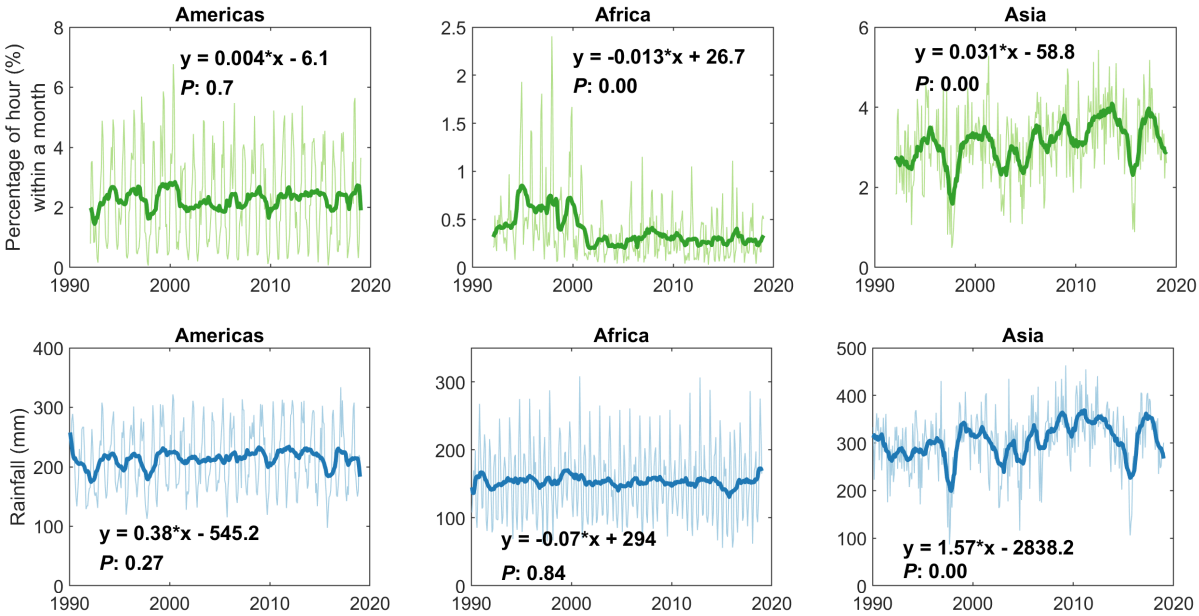

Fig. S23. (Top row) Dynamics of monthly leaf surface dew duration for American, African, and Asian intact tropical rainforests. Shown are the averages across all intact rainforest 25 km pixels. **(Bottom row)** Dynamics of monthly CHIRPS rainfall for American, African, and Asian intact tropical rainforests. The thin line in each panel shows the monthly rainfall or dew duration, and the thick line shows a 12-month moving average. A linear regression was fitted to the monthly rainfall or dew duration and the regression equation was labeled in each panel.

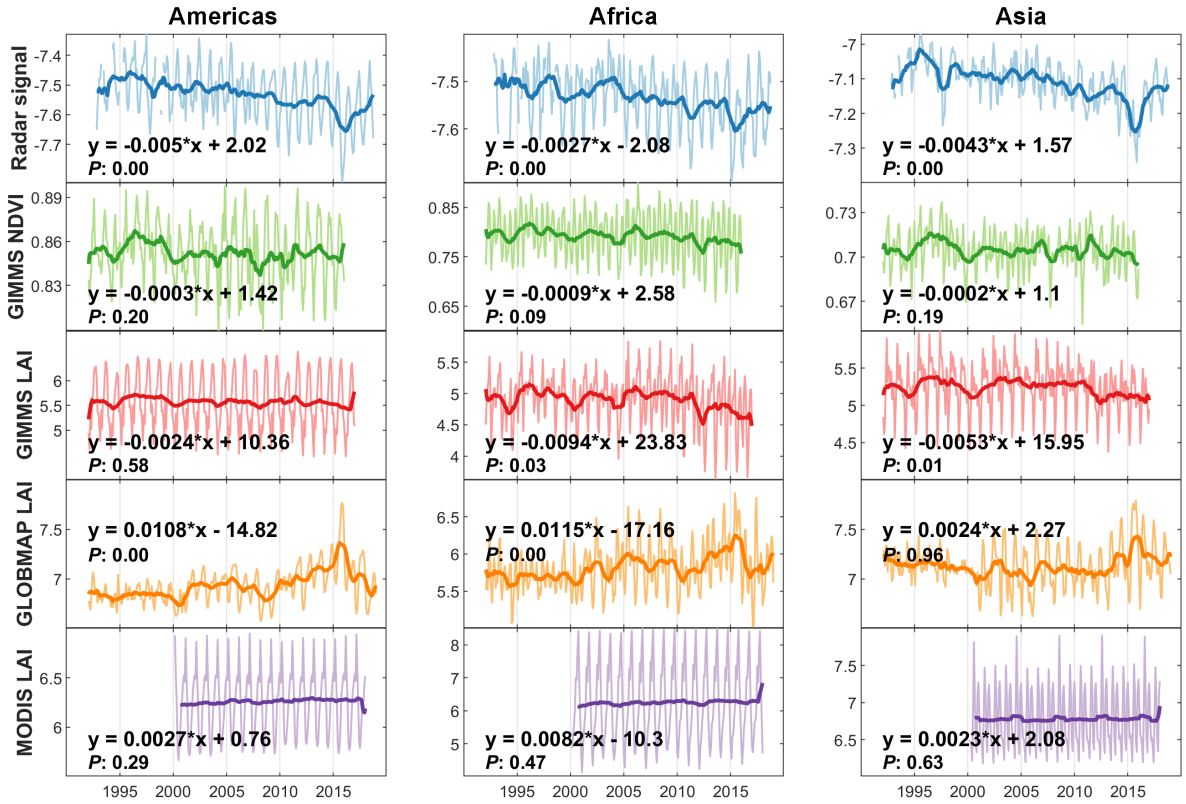

Fig. S24. Dynamics of monthly radar signal (top row), GIMMS NDVI (second row), GIMMS LAI (third row), GLOBMAP LAI (fourth row) and MODIS LAI (bottom row) in American, African, and Asian intact tropical rainforests. Shown are the averages across all intact rainforest 25 km pixels. In each subset, the monthly NDVI/LAI observation is shown as a thin line, on top of which a 12-month moving average is shown as a thick line. Linear regression was fitted to the monthly radar signal, NDVI or LAI, and the regression equation was labeled within each panel.

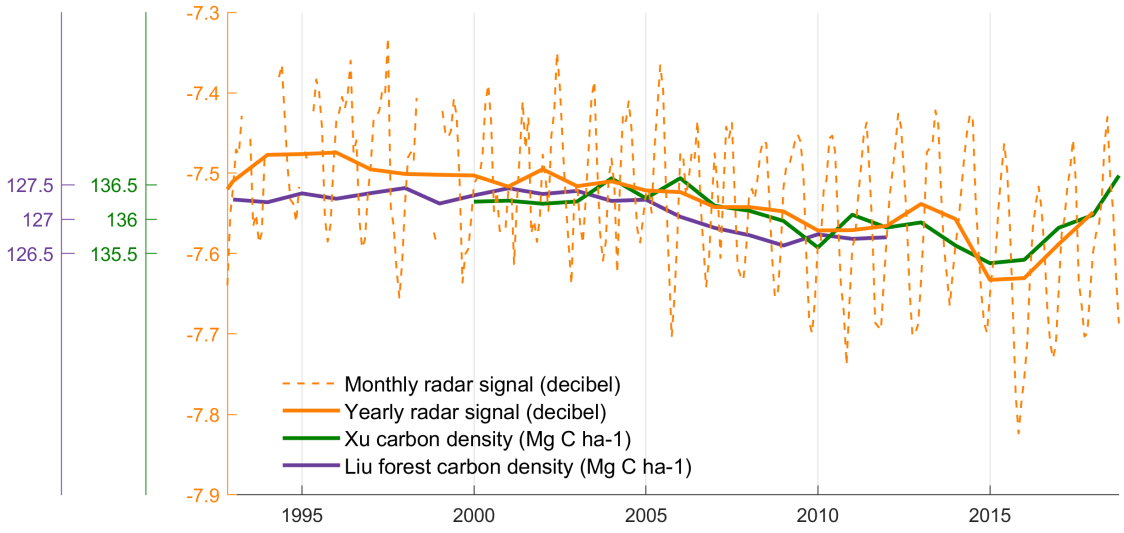

Fig. S25. Radar signal compared with time series of forest biomass carbon for the American tropics. Both the radar signal and forest biomass carbon shown here have been averaged across intact rainforest pixels within the American tropics. Time series of forest biomass carbon were taken from ref (*54*) and ref (*55*). The Pearson r between the yearly radar signal and Xu carbon density is 0.86 ($P < 0.01$). The Pearson r between the yearly radar signal and Liu carbon density is 0.84 ($P < 0.01$).

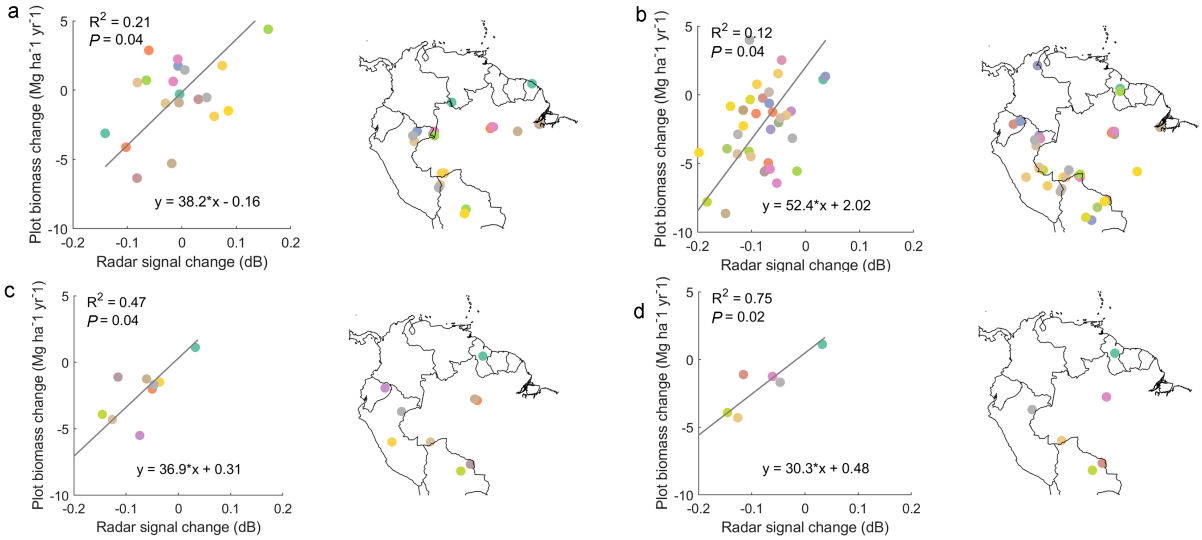

Fig. S26. Changes in radar signal *versus* changes in plot biomass during two mega-droughts. Significant positive correlations between radar signal changes and plot biomass changes were obtained, suggesting that the radar signals detect drought-induced biomass loss. (**a**) and (**b**) show the changes in the radar signal *versus* changes in plot biomass caused by the droughts of 2005 and 2010, respectively. (**c**) is similar to (b), but includes only radar pixels with at least two ground plots in the pixel footprint, and 5 km apart. (**d**) is similar to (c), but with a distance between plots at least 10 km. (c) and (d) attempted to solve the scale mismatch between the radar pixel (25 km) and the ground plot (~1 ha). The colours were randomly assigned to the points in each panel.

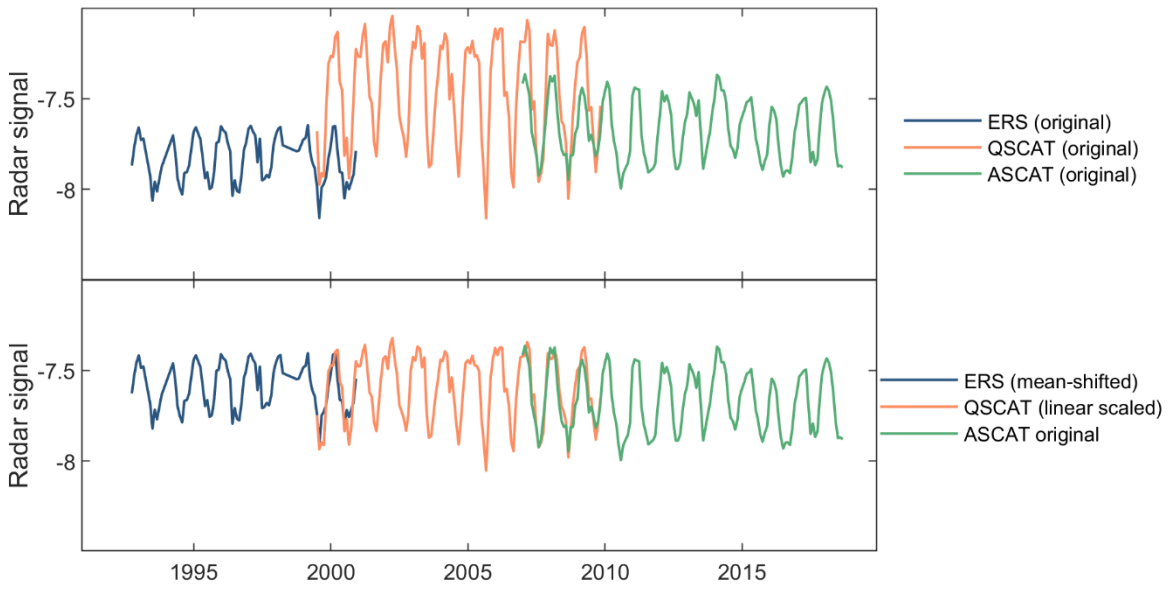

Fig. S27. Illustration of the rescaling of radar data from different sensors. The top panel shows the original time series prior to rescaling. The bottom panel shows the same time series but after rescaling.

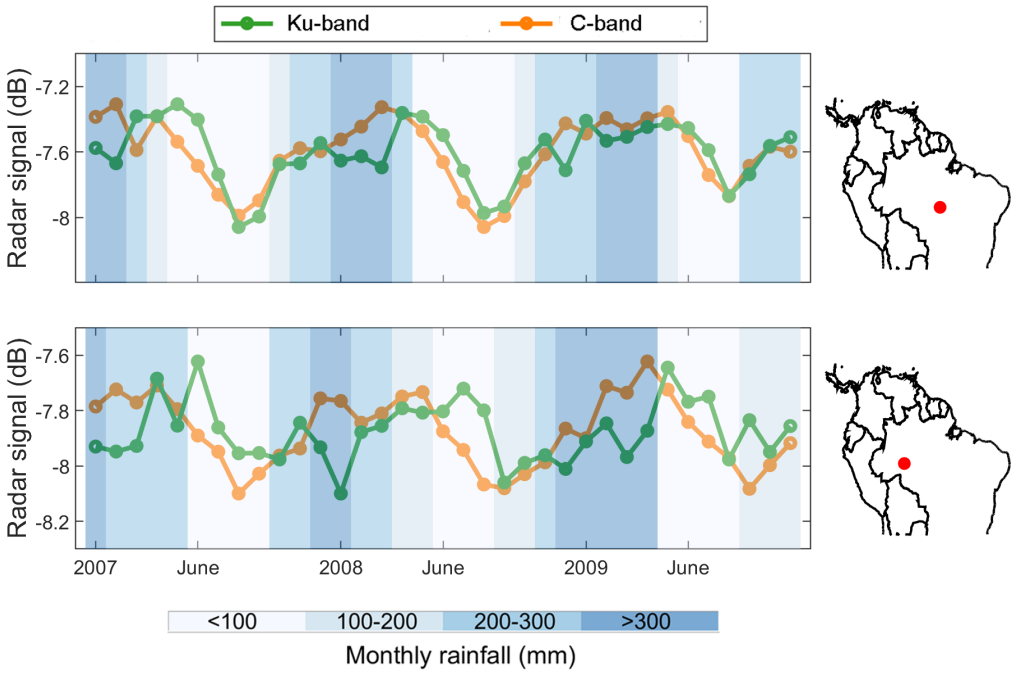

Fig. S28. Comparisons between Ku-band (QSCAT) and C-band (ASCAT) radar signals over a 3-year overlapping period (2007-2010). The signals are from two pixels with different annual precipitations as measured by TRMM 3B43 V7 data. Pixel locations are shown as red dots in the right panels.

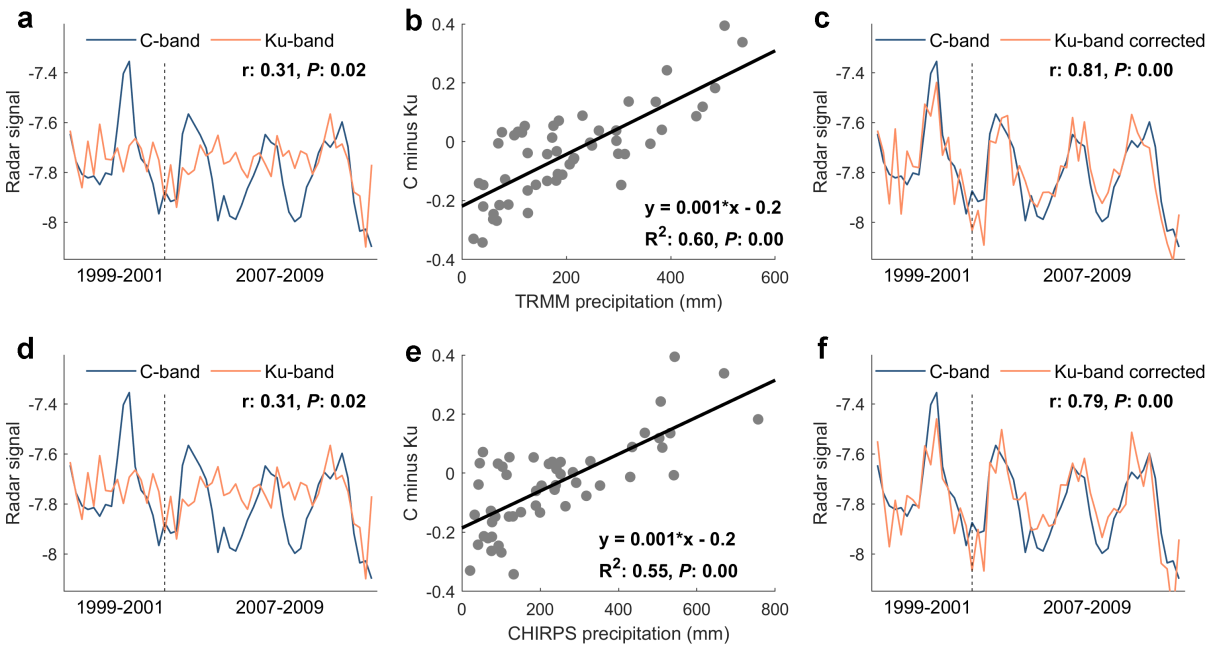

Fig. S29. Illustration of the rainfall-assisted correction on Ku-band (QSCAT) signals. a, C-band and Ku-band signals before correction. **b**, regression between signal differences and TRMM precipitation. **c**, C-band and Ku-band signals after correction. The vertical dotted line in **a** and **c** separates the ERS-QSCAT overlapping (1999–2001) and QSCAT-ASCAT (2007–2009) overlapping periods. **(d-f)** show the same Ku-band signal but corrected by CHIRPS rainfall.

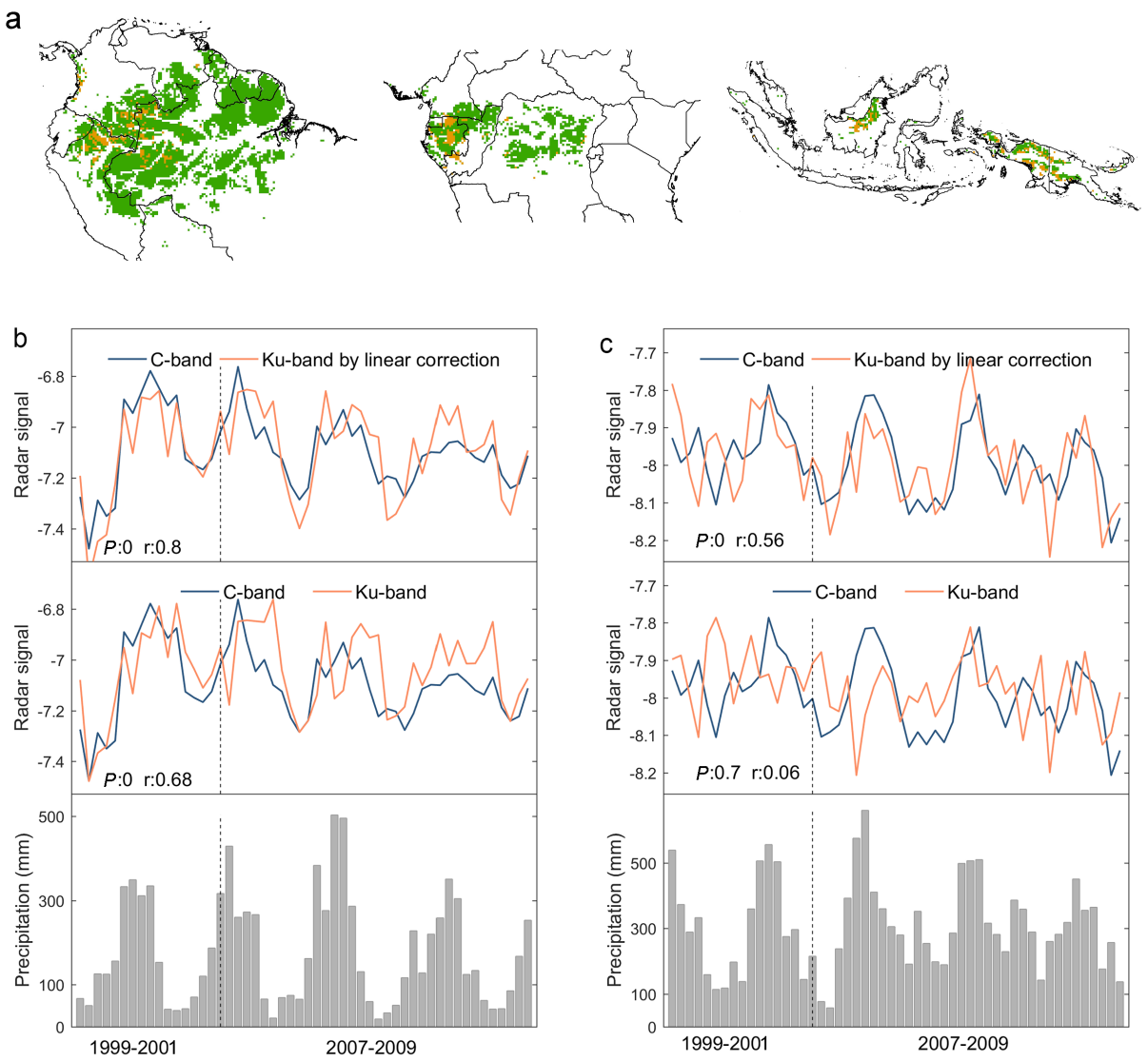
a
b
C-band
Ku-band by linear correction
Radar signal
-6.8
-7
-7.2
-7.4
P:0 r:0.8
C-band
Ku-band
Radar signal
-6.8
-7
-7.2
-7.4
P:0 r:0.68
Precipitation (mm)
500
300
100
0
1999-2001
2007-2009
c
C-band
Ku-band by linear correction
Radar signal
-7.7
-7.8
-7.9
-8
-8.1
-8.2
P:0 r:0.56
C-band
Ku-band
Radar signal
-7.7
-7.8
-7.9
-8
-8.1
-8.2
P:0.7 r:0.06
Precipitation (mm)
500
300
100
0
1999-2001
2007-2009

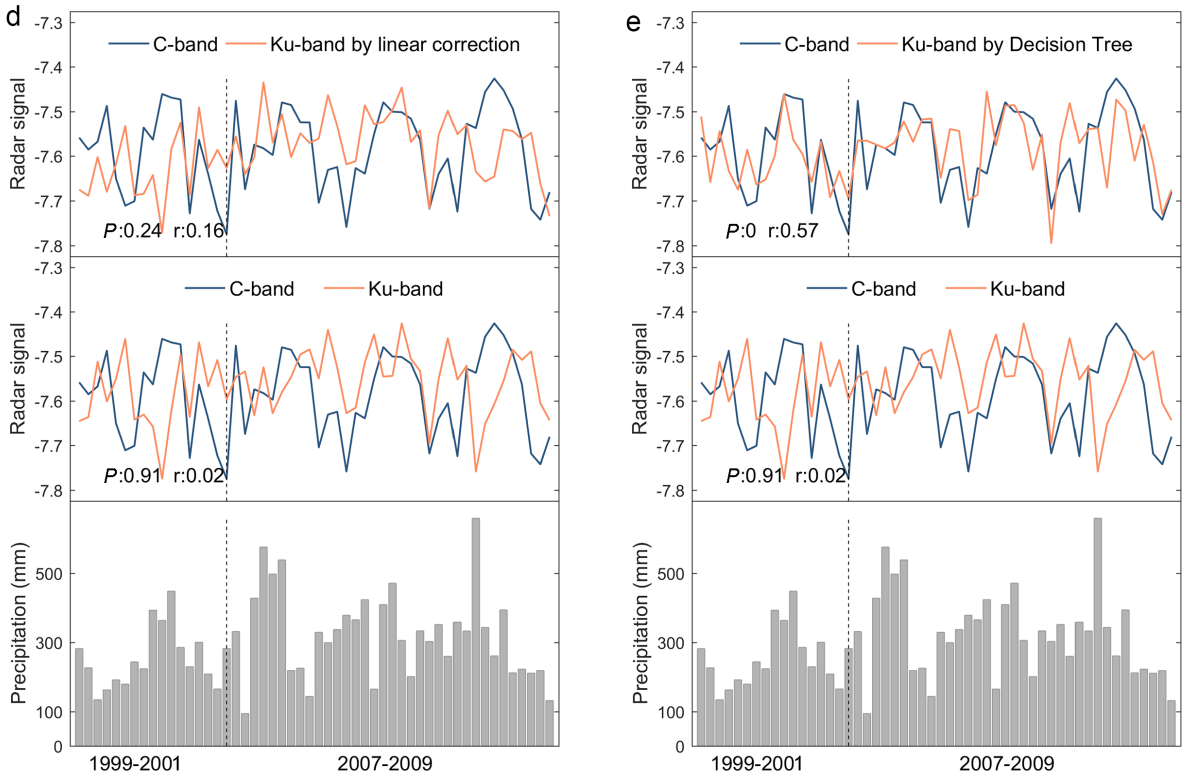

Fig. S30. Spatial pattern and examples of the rainfall-assisted correction on Ku-band signals. a. Two regions (distinguished by colour) where rainfall-assisted correction on the Ku-band signal was made using different regression techniques. In the region coloured green, linear regressions were performed between the signal differences and the precipitation (i.e., linear regression correction). In the region coloured yellow, a decision tree analysis was performed between the signal differences and the precipitation (i.e., Decision Tree regression correction). **b & c.** Two examples of the rainfall-assisted correction in the "green" region. The match between the Ku-band and C-band signals was greatly improved after the correction. **d & e.** An example of the rainfall-assisted correction in the "yellow" region. Precipitation is less seasonal in this region, so linear regression between signal differences and precipitation did not improve the match between the two signals (**d**). Decision tree analysis was finally used to model the signal differences from rainfall amounts; this improved the match (**e**).

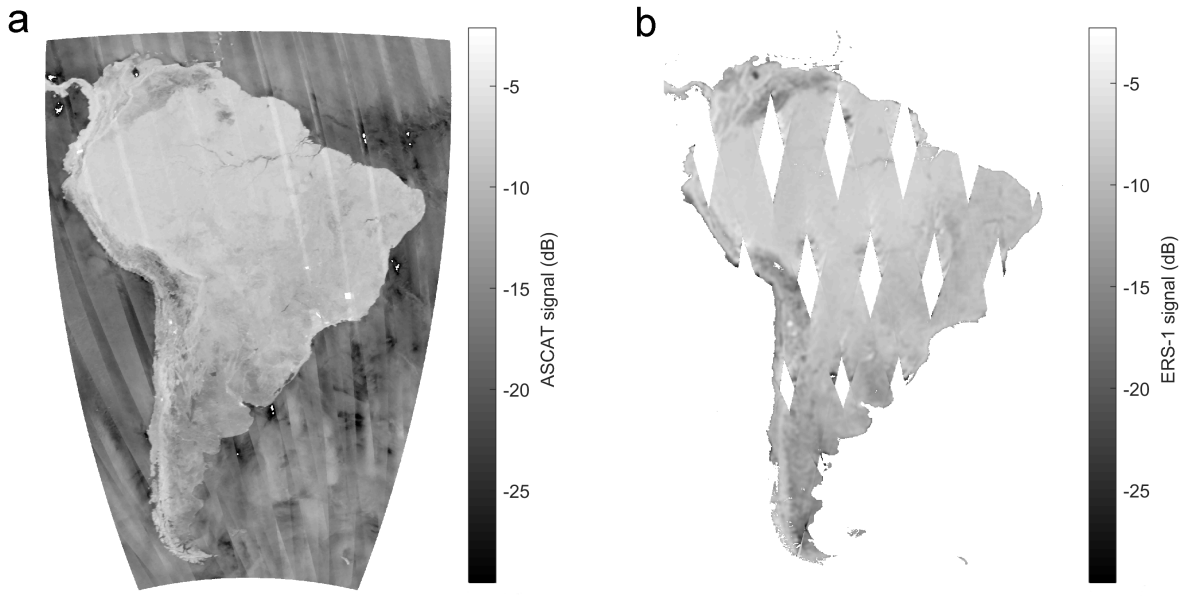

Fig. S31. (a) An example of ASCAT image with data strips (light gray strips in the image) acquired in May 2010, and **(b)** an example of a low-quality ERS-1 image acquired in March 1992.